Geophysical Journal International

Geophys. J. Int. (2018) **215,** 1701–1717
Advance Access publication 2018 September 03
GJI Geomagnetism, rock magnetism and palaeomagnetism

doi: 10.1093/gji/ggy361

A Late-Quaternary full-vector geomagnetic record from El Golfo section, El Hierro, Canary Islands

Marilyn W.L. Monster,[1,2] Joris van Galen,[1] Klaudia F. Kuiper,[2] Mark J. Dekkers[1] and Lennart V. de Groot[1]

[1] *Paleomagnetic Laboratory 'Fort Hoofddijk', Department of Earth Sciences, Utrecht University, Budapestlaan* 17, 3584 *CD Utrecht, The Netherlands. E-mail: l.v.degroot@uu.nl*

[2] *Geology and Geochemistry Cluster, Faculty of Earth and Life Sciences, Vrije Universiteit Amsterdam, De Boelelaan* 1085, 1081 *HV Amsterdam, The Netherlands*

Accepted 2018 August 30. Received 2018 August 24; in original form 2018 July 04

SUMMARY

Regional full-vector palaeosecular variation (PSV) curves are essential to further our understanding of geodynamo operation. Such curves typically lack palaeointensity information (with palaeodirectional being much more common), particularly for periods before the Holocene. Notably low palaeointensity values have been reported for significant portions of the Late Quaternary. Here, we present full-vector palaeomagnetic from the El Golfo section on El Hierro (Canary Islands, Spain), spanning the age range between ∼120 and ∼450 ka, to substantiate these reported low palaeointensity values for the Canary Islands. We sampled 28 flows (mostly alkaline oceanic basalts of the shield building stage) along the Camino de Jinama, a few kilometres to the south of a section studied by Széréméta *et al.* for PSV. In line with their results, we observe an easterly declination deviation of ∼14° for the middle and lower part of our section. We relate this to undersampling of the complete PSV spectrum; rotation of El Hierro since ∼500 ka is deemed unlikely. Attempts to date the flows with the $^{40}Ar/^{39}Ar$ method on a multi-collector instrument were unsuccessful due to the presence of copious amounts of methane in the extracted gases. Stratigraphic correlation to Széréméta *et al.*'s section lends support to ages (technically of very low quality) obtained for the sites reported on here. Importantly, we add palaeointensity information in the present study, for the first time on El Hierro. Three different palaeointensity protocols were utilized, IZZI-Thellier, multispecimen, and pseudo-Thellier, to provide an additional consistency check and to increase the success rate. After applying strict selection criteria, reliable palaeointensities could be obtained for 18 flows, a success rate of ∼64 per cent. If more than one protocol yielded results for the same flow, the obtained intensities were often within error of each other, testifying to their robustness. Flows with a common true mean direction tend to produce similar intensity values as well; this testifies to the presumed under-sampling of PSV within the section. Obtained palaeointensity values typically range between ∼20 and ∼35 μT, distinctly lower than the present-day field value of ∼39 μT and lower than the average intensity during the Brunhes Chron. The determinations are in line with other rather low values obtained elsewhere for this particular time span.

Key words: Palaeointensity; Palaeomagnetic secular variation; Palaeomagnetism; Physics and chemistry of magma bodies.

1 INTRODUCTION

The Earth's magnetic field is generated in the liquid outer core of the planet by processes referred to as the geodynamo. The field has a higher propensity to reverse polarity when its intensity is low, usually estimated at corresponding dipole moments $<\sim 4\times10^{22}$ Am^2 (e.g. Valet *et al.* 2005; Channell *et al.* 2009). This is deduced from calibrated relative palaeointensity records which are always inherently smoothed to a certain degree, apart from potential issues related to the calibration. Other workers (Lawrence *et al.* 2009; Cromwell *et al.* 2015) consider 4×10^{22} Am^2 within the range of the stable dipole moment; even lower dipole moments would be required for the field being prone to reverse. So-called absolute palaeointensities, that is field intensities in μT for a given location that can be converted to a virtual (axial) dipole moment, are tedious to obtain and therefore remain rather scarce, in particular for periods

© The Author(s) 2018. Published by Oxford University Press on behalf of The Royal Astronomical Society.

Downloaded from https://academic.oup.com/gji/article-abstract/215/3/1701/5090145 by Universiteitsbibliotheek Utrecht user on 12 February 2019

older than the Holocene (*cf.* compilations by Knudsen *et al.* 2008; Ziegler *et al.* 2008, 2011). The average field intensity over the last millions of years is considered to be lower than the current field, with the Holocene field intensity being high. This most recent past 10 kyr are reasonably well constrained by data from lavas and archaeological artefacts at least for considerable portions of the northern hemisphere as illustrated by, for example the CALS family of geomagnetic field models (Korte *et al.* 2009, 2011). While the average intensity of the Brunhes Chron is ∼20 per cent higher than most of the underlying Matuyama Chron (Ziegler *et al.* 2011), longer term trends within the Brunhes Chron, however, are surprisingly poorly characterized. It seems that the period between ∼200 and ∼400 ka featured a lower field intensity as determined for Hawaii (e.g. Tauxe & Love 2003) but data paucity precludes firm inferences. To contribute to this issue we recently revisited sites in the Eifel (Germany) and provided multimethod palaeointensity data for a set of lava flows (Monster *et al.* 2018) validating earlier estimates of Schnepp *et al.* (1995, 1996). It should be realized that ages of the lavas may come with a fairly large uncertainty, therefore improving on age determinations is also a prerequisite to progress. The inherent resolution of radiometric dating, however, will always be an issue given the high precision required for geomagnetic applications. Statistically establishing whether directional groups exist in data from a stack of lava flows remains mandatory for a meaningful interpretation in terms of geomagnetic field behaviour.

In this contribution, we present new data from El Hierro, Canary Islands. We sampled 28 lava flows (age range ∼450 to 120 ka) at a section along the Camino de Jinama, about 4.5 km to the south of a section sampled by Széréméta *et al.* (1999) for an analysis of directional palaeosecular variation. No palaeointensity results have been published for lavas from El Hierro to date. Palaeomagnetic directions from El Hierro, including two from Camino de Jinama, were published by Guillou *et al.* (1996). Palaeointensity studies on other islands in the Canary archipelago include work on historical and Holocene lavas (e.g. Soler *et al.* 1984; de Groot *et al.* 2015; Kissel *et al.* 2015; Monster *et al.* 2015a; Calvo-Rathert *et al.* 2016), and on the periods around the Matuyama-Brunhes and other polarity transitions (e.g. La Palma: Quidelleur & Valet 1996; Valet *et al.* 1999; Tenerife: Kissel *et al.* 2014; La Gomera: Caccavari *et al.* 2015; Lanzarote: Calvo-Rathert *et al.* 2016) and geomagnetic field excursions (e.g. Quidelleur *et al.* 1999; Singer *et al.* 2002). Previous radiometric ages from El Hierro were mostly obtained using the K/Ar method (Abdel-Monem *et al.* 1971, 1972; Fúster *et al.* 1993; Guillou *et al.* 1996; Széréméta *et al.* 1999). Longpré *et al.* (2011) dated four lava flows that straddle the most recent flank collapse using the $^{40}Ar/^{39}Ar$ method bracketing its age between ∼85 and ∼40 ka, distinctly younger than hitherto assumed.

Here we integrate rock magnetic and palaeomagnetic experiments using a multimethod palaeointensity approach with radiometric dating. Three different palaeointensity methods are used: the IZZI-Thellier protocol (e.g. Tauxe & Staudigel 2004; Yu & Tauxe 2005), the multispecimen protocol (Dekkers & Böhnel 2006; Fabian & Leonhardt 2010) and the calibrated pseudo-Thellier approach (de Groot *et al.* 2013, 2016). This multimethod approach enhances the (usually low) success rate of palaeointensity experiments. Moreover, consistency between results from different methods provides an important additional reliability check (see also de Groot *et al.* 2013, 2015; Monster *et al.* 2015a; Calvo-Rathert *et al.* 2016, 2016). In an effort to constrain the age range of the sampled flows, seven flows were selected for $^{40}Ar/^{39}Ar$ dating on the ThermoFisher Helix MC multicollector mass spectrometer at the Vrije Universiteit Amsterdam (The Netherlands). Its unprecedented resolution should enable to precisely date comparatively young rocks with ages of less than 500 ka.

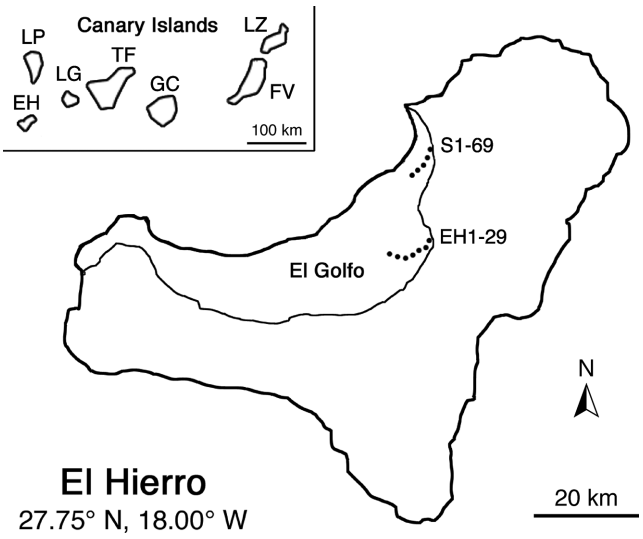

Figure 1. El Hierro and the Canary Islands. El Hierro (EH) is the most westerly of the Canaries. The other islands are (from west to east) La Palma (LP), La Gomera (LG), Tenerife (TF), Gran Canaria (GC), Fuerteventura (FV) and Lanzarote (LZ). The dashed lines indicate our section, Camino de Jinama (EH1-29), and Széréméta *et al.* (1999)'s section a few kilometres to the north (S1-69) along the El Golfo scarp.

2 GEOLOGICAL SETTING AND SAMPLING

The Canary Islands are part of the Canary Island Seamount Province (CISP) which comprises more than 100 seamounts and a collection of islands off coast NW Africa. The CISP developed on ancient ocean crust, the oldest Atlantic Ocean crust Jurassic in age, relatively close to the continent of Africa. El Hierro is the smallest and most westerly of the Canary Islands archipelago (Fig. 1) believed to have formed at the present location of the Canaries hot spot (Holik *et al.* 1991). Some of the seamounts are considerably older than previously thought indicating a protracted hot spot history with several recurrent episodes of 'low production' hotspot activity with a shallow source (van den Bogaard 2013). Recent geophysical-petrological lithosphere modelling (Fullea *et al.* 2015) infer a strong, non-thinned lithosphere under the CISP and an enriched shallow mantle under El Hierro, La Palma and Lanzarote (Hoernle *et al.* 1991). The islands were formed in a relatively short time span. El Hierro lies slightly west from the top of an ancient seamount (133 Ma), the El Hierro Ridge Seamount (van den Bogaard 2013).

El Hierro and La Palma represent the youngest islands with ages of <2 Ma (Guillou *et al.* 1996; Carracedo *et al.* 1999; Tauxe *et al.* 2000). They are currently in the so-called declining stage of the Canary Island volcanic sequence. El Hierro has a typical trilobate shape, the result of three main phases of eruptive activity during the shield building phase. Landslides played a critical role in shaping the island (e.g. Carracedo *et al.* 1999; Gee *et al.* 2001). All cliff-bound basins are related to collapse structures. On El Hierro, the oldest subaerial volcanism of the El Tinor edifice was dated at 1.12 Ma (Guillou *et al.* 1996). This volcanic edifice developed quickly, until the northwest flank of the volcanic edifice collapsed at ∼880 ka (Guillou *et al.* 1996). The next stage of development was the El

Downloaded from https://academic.oup.com/gji/article-abstract/215/3/1701/5090145 by Universiteitsbibliotheek Utrecht user on 12 February 2019

Golfo edifice, which formed between approximately 545 and 176 ka (Guillou *et al.* 1996). Its north flank collapsed in one (Masson 1996; Masson *et al.* 2002) or more (Carracedo *et al.* 1999) landslides, creating the spectacular El Golfo valley and scarp. The most recent phase of volcanic activity consists of Rift volcanism (Carracedo *et al.* 2001) that has been dated to 145 to 2.5 ka (Guillou *et al.* 1996). Very recently in 2011, a submarine eruption occurred near La Restinga (Carracedo & Troll 2016).

The Canary Islands can be grouped according to the alkalinity of their basalts which is rather constant for each island. The shield-building stage basalts of El Hierro, that is most rocks on the island, are alkaline oceanic basalts. They are moderately alkaline; La Palma and Tenerife are more alkaline (Carracedo *et al.* 2002). Very young Rift volcanism rocks on El Hierro comprise trachytes and phonolites, typical of the declining stage.

We sampled a total of 28 lava flows from the El Golfo and Rift volcanism phases, located along the Camino de Jinama (EH1-29, dotted line in Fig. 1). Sites EH5 and EH15 were numbered but not sampled, EH8 was sampled at two different levels that may be two separate events. The sampled section starts at about 1250 m a.s.l. down to approximately 700 m. a.s.l. The section is ∼4.5 km to the south of the section sampled by Szériméta *et al.* (1999) (S1–69 in Fig. 1). The section's schematized stratigraphy is shown in Fig. 2. Flows, ranging in thickness between 1 and several metres, were usually easily distinguished by the presence of scorias, pyroclastic layers or palaeosols in between the solid cooling units. The latter indicate some more time between successive flows given the fair amount of time needed for developing a soil, also under fairly moist climate conditions that prevail on the windward northwest coast.

We divided consecutive flows into three groups, referred to as the upper group (UG, consisting of flows EH1 to EH4), the middle group (MG, EH7 to EH12) and the lower group (LG, EH16 to EH29). Between these groups, isolated flows were sampled as well. A notably thick layer of pyroclastics separates EH4 from EH5, whereas appreciable palaeosols are visible between flows EH6 and EH7, flows EH15 and EH16, flows EH26 and EH27, and flows EH28 and EH29. Some less prominent palaeosols are indicated as well on Fig. 2.

The section is occasionally intruded by dykes. We sampled as far away from these as possible to reduce the risk of thermal overprinting of the flows. Fairly large parts of the section are covered by lush vegetation given the windward position on the northwest coast of the island. These parts (omitted from the volcanostratigraphic column in Fig. 2) may contain a substantial number of lava flows that cannot be sampled. Szériméta *et al.* (1999)'s stack, which overlaps in age with our section, consists of a larger number of flows: 69. Access to that section along Camino de la Peña was prohibited due to rock fall when we visited El Hierro in October 2014.

We took at least 15 cores (1-inch diameter) per flow using a petrol-powered portable drill; flows EH5 (dangerous drilling conditions) and EH15 (inaccessible) could not be sampled. The cores were oriented using a magnetic compass and if weather conditions permitted also a sun compass. Due to the often overcast weather, we only managed to obtain solar readings for 6 flows (EH2, EH3, EH14, EH21, EH24 and EH29). These sun compass readings generally deviated $<3^\circ$ (maximum <5) from the magnetic compass readings. As these deviations are not systematic we cannot correct for local magnetic anomalies influencing our compass readings, but the observed deviations are generally small. Cores were usually taken in several small clusters that were distributed laterally and vertically over several metres, while avoiding the top part of the flow that may have been reheated by the overlying flow. We also took hand samples for $^{40}Ar/^{39}Ar$ dating from seven flows: EH1, EH11, EH14, EH17, EH22, EH28 and EH29, spanning the entire section (Fig. 2).

3 PALAEOMAGNETIC DIRECTIONS AND ROCK MAGNETIC CHARACTERIZATION

3.1 Demagnetization of the NRM and palaeomagnetic directions

Palaeomagnetic directions were obtained using both thermal and alternating field (AF) demagnetization. Per site, three samples were thermally demagnetized using temperature steps of 50 °C between 100 and 500 °C and steps of 25 °C between 500 and 600 °C. Most specimens were measured on a 2 G DC-SQUID magnetometer; specimens that were outside the 2G's dynamic range were measured on an AGICO JR-6 spinner magnetometer. This occurred mainly for sites that had been remagnetized by lightning.

Five specimens per site were subjected to AF demagnetization using steps of 0, 2.5, 5, 7.5, 10, 15, 20, 25, 30, 40, 50, 60, 70, 80, 90 and 100 mT using a robotized 2 G DC-SQUID magnetometer in a static 3-axes demagnetization set-up (Mullender *et al.* 2016). Additionally, these samples were manually demagnetized at fields of 150, 225 and 300 mT, and measured on the robotized magnetometer. The robotized AF set-up results in significantly less scatter compared to the thermal data; it should be noted, however, that in the AF demagnetization experiment samples are fixed in a holder only once, hence positioning alignment errors are not averaged over consecutive steps. Samples whose NRM was outside the magnetometer's range were manually demagnetized and measured on a JR-6 spinner magnetometer using fewer steps: 0, 5, 7.5, 10, 12.5, 15, 20, 25, 35, 50, 70 and 100 mT. All demagnetization data were analysed using Palaeomagnetism.org (Koymans *et al.* 2016).

Palaeomagnetic directions could be obtained for 24 flows, the primary magnetization of flows EH9, EH10 and EH13 was fully overprinted. Also, some specimens from EH11 and EH12 immediately below EH9 and EH10 were affected by lightning to a lesser extent, as well as some specimens from EH7 (Supplementary Material A). The UG flows (EH1 to EH4) are characterized by small overprints in their AF Zijderveld diagrams that were removed by 5–15 mT. Their thermal demagnetization behaviour often appeared to be rather chaotic. Most MG and LG flows (EH7 to EH29) show univectorial demagnetization behaviour with essentially no overprints (Fig. 3, Table 1). The associated k-values are generally >50, which is often considered the minimum for a paleomagnetic direction from a single cooling unit (Table 1). The mean directions of flows EH1, EH7, EH11, EH12, EH17 do not meet this criterion; their directions are therefore not considered to be reliable spot readings of the geomagnetic field.XXXX

Like Szériméta *et al.* (1999) we found predominantly easterly directions (*cf.* Table 1): the UG flows all yielded declinations of ∼30°, combined with shallow inclinations that are on average 23.9°—a geocentric axial dipole would yield 46.5° at this latitude. Except for one, all MG palaeomagnetic directions with $k > 50$ exhibit easterly declinations of 4.3° to 16.1°, in combination with large variations in inclination (27.3° to 46.6°), albeit that these inclinations all are also low for the latitude of El Hierro. The LG palaeomagnetic directions that meet our k-criterion (EH16 to EH29) produced declinations of 4.3° to 22.8°, with inclinations close to a GAD, varying between 35.4° and 50.0°. The only westerly oriented flows with $k > 50$ are EH6 (dec = 350.5°), and EH8I (dec = 332.6°).

Downloaded from https://academic.oup.com/gji/article-abstract/215/3/1701/5090145 by Universiteitsbibliotheek Utrecht user on 12 February 2019

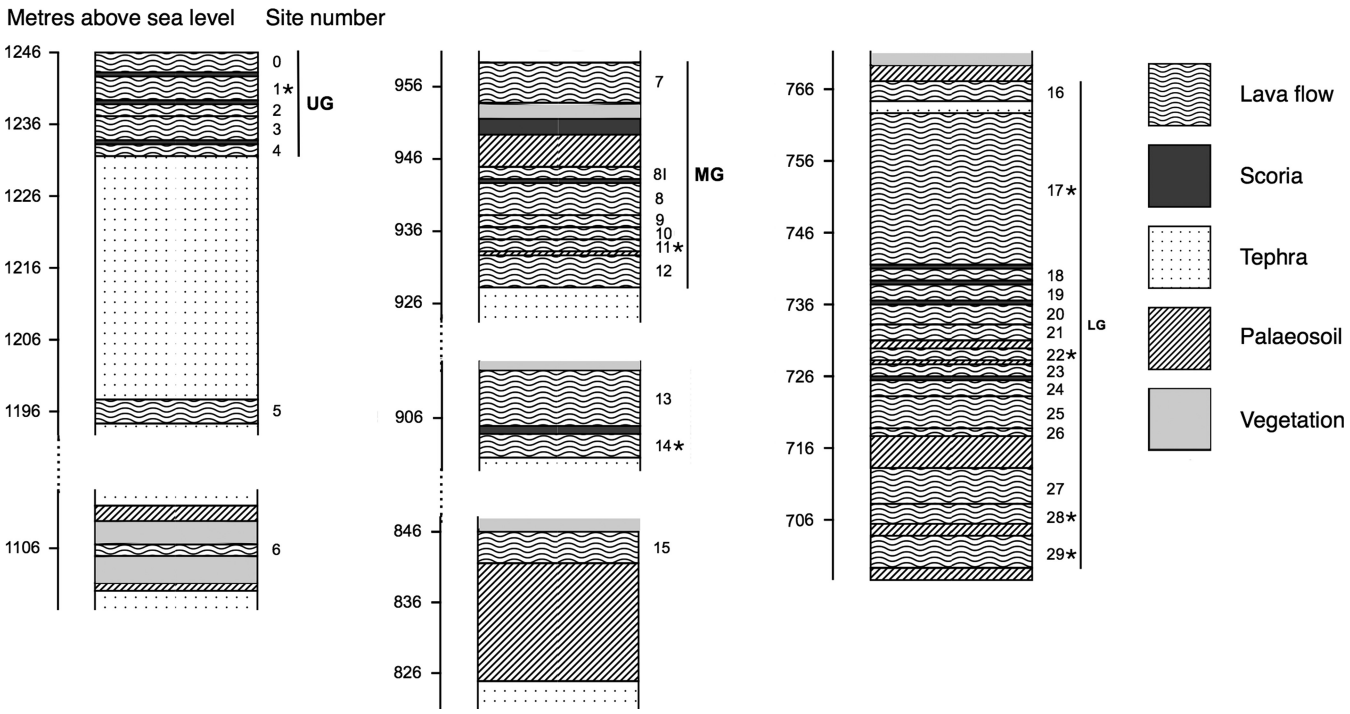

Figure 2. Stratigraphy of our section along Camino de Jinama. Large parts of the section were covered by vegetation and difficult to access and are not shown in this figure, apart from the few metres below EH7 (in white). The sites sampled for Ar/Ar dating are marked with ∗.

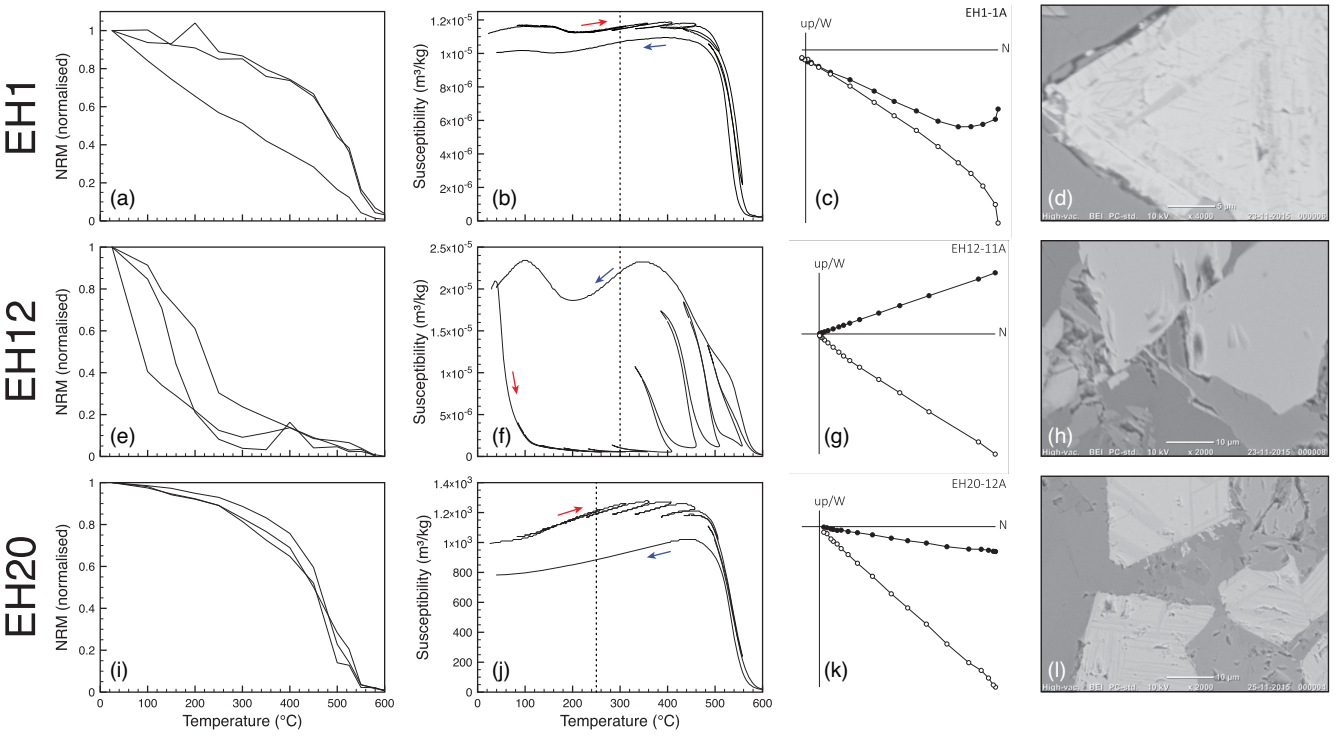

Figure 3. Rock-magnetic characterization. For three typical flows (UG: EH1, MG: EH12, and LW: EH20) the demagnetization spectra (for three samples each; A, E, I), susceptibility versus temperature analyses (B, F, J), Zijderveld diagrams (alternating field demagnetization; C, G, K), and Scanning Electron Microscopy (SEM) images (D, H, L) are provided. The dashed lines in the susceptibility versus temperature plots indicate the onset of alteration; red arrows indicate the initial heating cycle, blue arrows the final cooling segment. Closed dots in the Zijderveld diagrams are in the horizontal plane, open dots in the vertical plane. Based on the SEM images all sites were classified as oxidation class I, II, III or IV (Table 1).

Downloaded from https://academic.oup.com/gji/article-abstract/215/3/1701/5090145 by Universiteitsbibliotheek Utrecht user on 12 February 2019

Table 1. Palaeomagnetic directions and rock-magnetic results. For each site its stratigraphic group (Strat. Group, U: upper, M: middle, L: lower), location (UTM coordinates, zone 28R), palaeomagnetic directions [declination (dec), inclination (inc), $\alpha 95$, *k*-value (k) and number of specimens (N)] and some rock magnetic parameters [Curie (T_C) and alteration (T_{alt}) temperatures, and oxidation class (Ox.cl.) according to Watkins & Haggerty (1968)] are given. Four groups of consecutive sites (EH1 to EH4, EH18 to EH20, EH21 and EH22 and EH26 and EH27) pass a common true mean directions (CTMD) test, and their results are also interpreted as being one event (i.e. site). Sites fully remagnetized by lightning are marked with ^{L}, sites partly affected by lightning are marked with $^{(L)}$. The palaeodirections with an associated *k*-value <50 are deemed unreliable; these sites are marked with ^{k}. The sites sampled for Ar/Ar analyses are marked with∗.

		Location (UTM 28R)		Palaeomagnetic directions					Rock magnetic characterization		
Site	Strat. group	Northing	Easting	dec	inc	$\alpha 95$	*k*	*N*	T_c (° C)	T_{alt} (° C)	Ox. Cl.
EH1 ∗ ^{k}	U	206190	3074463	29.5	28.6	10.5	34.0	7	570	300–350	IV
EH2	U	206188	3074461	27.3	24.5	6.1	98.9	7	540	400–450	–
EH3	U	206173	3074441	34.4	20.1	4.7	139.9	8	540	450–500	–
EH4	U	206173	3074443	32.8	23	2.6	454.9	8	500	450–500	IV
EH1–4	**U**	**CTMD**		**31.2**	**23.9**	**3**	**77.7**	**30**			
EH6		206147	3074220	350.5	12.1	7.3	110.8	5	100, 570	300–350	II
EH7 ^{k}	M	205707	3073754	5	36.3	10.1	36.7	7	180, 400	300–350	II
EH8I $^{(L)}$	M	205661	3073719	332.6	70.1	7.7	99.7	5	570	250–300	–
EH8	M	205651	3073743	4.3	38.7	3.9	240.5	7	570	350–400	III
EH9 ^{L}	M	205639	3073747	–	–	–	–	–	60, 500, 570	400–450	–
EH10 ^{L}	M	205638	3073747	–	–	–	–	–	220	350–400	–
EH11 ∗ $^{k(L)}$	M	205635	3073742	5.5	46.6	8.2	46.6	8	< 100	300–350	I-II
EH12 $^{k(L)}$	M	205631	3073733	3.1	27.3	8.7	49.1	7	100	250–300	I-II
EH13 ^{L}		205599	3073704	–	–	–	–	–	570	300–350	–
EH14 ∗		205591	3073691	13.6	49.6	4.5	152.5	8	60, 570	300–350	III
EH16	L	205459	3073547	9.7	44.5	3.8	213.5	8	570	250–300	III-IV
EH17 ∗ ^{k}	L	205448	3073539	354.7	42.2	15.8	13.2	8	60, 570	300–350	II-III
EH18	L	205448	3073561	9.4	42.2	6.1	83.4	8	570	250–300	-
EH19	L	205449	3073556	6.8	40	1.9	1010.9	7	550	250–300	III
EH20	L	205447	3073560	7.4	43.2	4.8	159.1	7	570	250–300	III-IV
EH18–20	**L**	**CTMD**		**7.9**	**41.8**	**2.5**	**154.7**	**22**			
EH21	L	205442	3073560	11	50.5	4	228.7	7	570	250–300	III-IV
EH22 ∗	L	205435	3073557	8	46.3	4.2	207.5	7	570	300–350	I-II
EH21–22	**L**	**CTMD**		**9.4**	**48.4**	**2.9**	**188.8**	**14**			
EH23	L	205435	3073558	13	42.5	3.3	282.7	8	540	350–400	I-II
EH24	L	205437	3073558	14.9	35.4	4.1	183.5	8	570	400–450	I-II
EH25	L	205437	3073556	22.8	37.3	4.4	159.5	8	570	300–350	II
EH26	L	205432	3073547	6.7	42.3	5.5	102.4	8	540	350–400	I
EH27	L	205417	3073539	8.1	43.2	3.4	266.4	8	570	400–450	II-III
EH26–27	**L**	**CTMD**		**7.4**	**42.7**	**3**	**152.2**	**16**			
EH28 ∗	L	205412	3073534	21.7	45.7	4.6	213.1	6	570	250–300	III
EH29 ∗	L	205403	3073529	4.3	39.5	4.3	166.9	8	570	400–450	II

3.2 Rock magnetic and microscopic characterization

All sites were rock magnetically characterized in detail before the start of the palaeointensity experiments. Information on the sites' magnetic domain state, alteration temperatures and Curie temperatures (T_C) are used to optimize the temperature steps in the Thellier-Thellier experiments and to choose suitable temperatures for the multispecimen experiments. Alteration and Curie temperatures were determined from susceptibility-versus-temperature diagrams measured on an AGICO KLY-3S susceptometer with a CS-3 furnace attachment. Susceptibility was measured during nine temperature cycles up to 600 °C, each cycle increasing the temperature by 100 °C and subsequently cooling by 50 °C. We define the alteration temperature as the highest temperature reached in the last thermal cycle that shows reversible behaviour. Curie temperatures (Fig. 3, Table 1, Supplementary Material A) were determined from the inflection point or points of the diagrams.

The UG and LG samples are characterized by high (>500 °C) Curie temperatures and alteration temperatures between 250° and 450° C. The MG samples are more variable: sites EH7, EH10, EH11 and EH12 have low to very low (100–200 °C) Curie temperatures, whereas sites EH8I, EH8 and EH9 have Curie temperatures of 570 °C. EH9 shows a second, very low Curie temperature of ∼60 °C (Table 1, Fig. 3, Supplementary Material A).

Magnetic domain states were assessed by measuring hysteresis loops and back-field curves on a MicroSense vibrating sample magnetometer (VSM). One 8-mm diameter sample (height ∼8 mm) per site was measured. The maximum field applied in the hysteresis loops was 1.5 T. We applied a slope correction to remove the paramagnetic contribution. From these measurements the saturation remanent magnetization M_r, the saturation magnetization M_s and the coercive field B_c were determined. The coercivity of remanence B_{cr} was obtained from a back-field remanence curve. The M_r/M_s and B_{cr}/B_c ratios were plotted on a Day plot (Day *et al.* 1977). Most sites plot within the pseudo-single-domain (PSD) range, with EH11 being close to single domain with a M_r/M_s of 0.44 (Fig. 4). EH6, two MG sites (EH7 and EH12), as well as two LG sites (EH24 and EH29) show B_{cr}/B_c ratios >5 and could be considered multidomain, although their M_r/M_s values vary between 0.09 and 0.19 and are relatively high for multidomain behaviour.

Downloaded from https://academic.oup.com/gji/article-abstract/215/3/1701/5090145 by Universiteitsbibliotheek Utrecht user on 12 February 2019

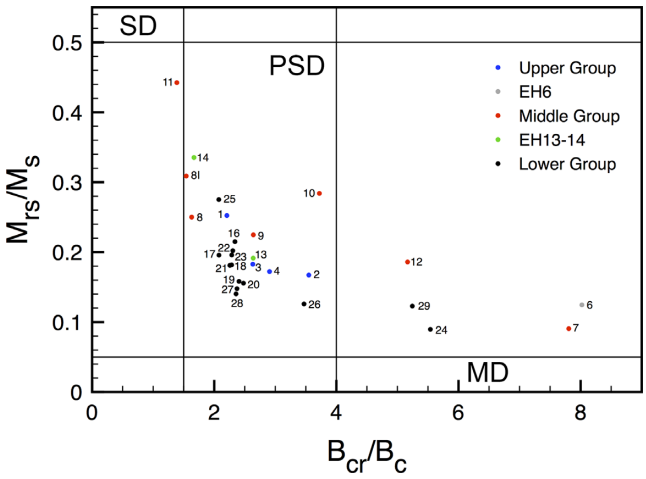

Figure 4. Day plot. Almost all sites are in the pseudo-single domain (PSD) realm, with the exception of site EH11 that is close to the single domain range (upper left), and sites EH6 and EH 7 that have very high B_{cr}/B_c ratios (∼8) and are therefore considered to be multidomain. Sites EH12, EH24 and EH29 are also close to the multidomain range (lower right).

To check for oxidation and exsolution, thin sections were examined with a JEOL JCM-6000 table-top scanning electron microscope (SEM) in backscatter mode; acceleration voltage was 10 kV. Images were taken at magnifications of up to 4000. Sites were categorized in oxidation classes (Table 1, Fig. 3, Supplementary Material B); they exhibit variable behaviour [oxidation classes I–IV according to Watkins & Haggerty (1968)]. For example, sites EH12 (MG) and EH29 (LG) show no or negligible oxidation and exsolution, whereas abundant ilmenite lamellae are visible in the SEM images of EH28 (LG). UG sites EH1 and EH4 show mottled lamellae and/or colour differences within their magnetite grains, placing them in oxidation class IV.

The seven flows that were prepared for $^{40}Ar/^{39}Ar$ dating (EH1, 11,14, 17, 22, 28 and 29) were also studied with an optical microscope. These images revealed plagioclase, olivine and pyroxene phenocrysts. Some volcanic glass was observed as well. Site EH28 (LG) consists of much finer grained material than the other six flows, and contains more volcanic glass than the other sites, which could pose problems for $^{40}Ar/^{39}Ar$ dating.

4 PALAEOINTENSITY EXPERIMENTS

4.1 IZZI-Thellier technique

For each site five samples were initially subjected to the IZZI-Thellier protocol (Tauxe & Staudigel 2004) with pTRM checks (Coe 1967). Depending on the site's Curie temperature and thermal demagnetization behaviour we used steps of 50 °C between 100 and 600 °C (samples with high T_C) or steps of 40 °C from 80 up to 480 °C (samples with lower T_C), the bias field was set to 40 μT. Subsequently, we measured an additional 2–5 samples using the same protocol, but with more optimized temperature steps (only minor changes compared to the original IZZI runs) and a bias field of 50 μT, for the most promising sites. In total 190 samples were processed. The data were analysed with ThellierGUI (v. 3.13) using the auto-interpreter function to make the data interpretation as objectively as possible (Shaar & Tauxe 2013). As there are many sets of selection criteria described in the literature and none of them stands out as superior over the others (Paterson *et al.* 2014), we ran the auto-interpreter with six different sets of criteria: PICRIT03, emphasizing the cumulative behaviour of the pTRM checks (Kissel & Laj 2004); SELCRIT2, with more weight on the directional behaviour during the Thellier experiment (Biggin *et al.* 2007); TTA and TTB, with emphasis on the quality of the pTRM checks (Leonhardt *et al.* 2004); all as modified by Paterson *et al.* (2014). Furthermore, we apply CROMWELL15 (Cromwell *et al.* 2015) that includes a check for the curvature of the Arai diagram; and Class A (de Groot *et al.* 2014), that focusses on the fraction of the Arai diagram interpreted. The CROMWELL15 set is by far the strictest, and is the only one to include a criterion to test for the curvature of the Arai diagram. We therefore impose an additional—rather loose—criterion to assess the curvature of the fit of the Arai diagram on all sets of criteria: k' (as defined by Paterson 2011) <0.35 (Table 2). For our 190 measured samples, 64 individual samples produced interpretations that passed either one of these selection criteria; from these a total 1387 interpretations could be made (see examples in Fig. 5, Table 3, Supplementary Table S1). One interpretation passed CROMWELL15, 48 passed modified TTA, 140 passed modified TTB, 321 passed modified PICRIT03, 344 passed modified SELCRIT2 and 160 passed Class A. Of course, there are interpretations that pass multiple sets of selection criteria; these doublings were left in the set of interpretations. With that, a single interpretation passing more sets of selection criteria (emphasizing different characteristics of the Arai interpretations) gets more weight in the averaging per site in the end.

At site level, we only accepted an average if it is the result of interpretations from at least three different samples, and the standard deviation divided by the palaeointensity is <20 per cent. For the sites with a common true mean direction the IZZI-Thellier intensity is also calculated as if these sites were indeed just one. We obtain an IZZI-Thellier average for 7 out of our 28 sites. The 4 UG sites produce consistently very low palaeointensities, with an average palaeointensity of 8.4 ± 1.4 μT. The other sites yield palaeointensities ranging from 19.2 to 40.8 μT, except for site EH25, that yields a palaeointensity of 61.7 μT.

4.2 Multispecimen experiments

The second palaeointensity technique that we applied is the domain-state-corrected multispecimen (MSP-DSC) protocol (Fabian & Leonhardt 2010). This extended protocol adds three heating steps to the original multispecimen protocol proposed by Dekkers and Böhnel in 2006 (MSP-DB). The measurement temperatures were chosen below the sites' alteration temperatures as determined from susceptibility-versus-temperature diagrams. As a further check for subtle magnetic alteration at the selected temperature, we applied the ARM test (de Groot *et al.* 2012). In this test, one core per site is heated in zero field to the intended MSP temperature, whereas a second core remains pristine. The samples are not to be AF demagnetized prior to the ARM acquisition as it is known that a preliminary AF demagnetization removes subtle, but important signs of alteration from the samples (de Groot *et al.* 2012). If the ARM acquisitions of the heated samples are equal to those of the pristine samples their acquisition behaviour was not altered by a thermal step; hence the MSP method is expected to yield the correct palaeointensity at that temperature. The ARM test, however, does not check for progressive thermal alteration, that is alteration that only occurs or worsens after more than one thermal cycle, such as the additional steps necessary for the MSP-DSC protocol. The MSP-DSC protocol has an inherent check for alteration, ε_{alt}, and

Downloaded from https://academic.oup.com/gji/article-abstract/215/3/1701/5090145 by Universiteitsbibliotheek Utrecht user on 12 February 2019

Table 2. IZZI-Thellier selection criteria. Six sets of selection criteria were used in this study: PICRIT03 (Kissel & Laj 2004), SELCRIT2 (Biggin *et al.* 2007), TTA, TTB (Leonhardt *et al.* 2004), as modified by Paterson *et al.* (2014); and CROMWELL15 (Cromwell *et al.* 2015), and Class A (de Groot *et al.* 2014). The different criteria are outlined in the Standard Palaeointensity Definitions (Paterson *et al.* 2014).

criterion	TTA mod (TTA)	TTB mod (TTB)	SELCRIT2 mod (S)	PICRIT03 mod (P)	CLASS A (A)	Cromwell15 (C)
n	≥5	≥5	≥4	≥4	≥7	
f	≥0.35	≥0.35	≥0.35	≥0.35	≥0.7	
β	≤0.10	≤0.15	≤0.10	≤0.10	≤0.10	≤0.10
q	≥5		≥1	≥1	≥5	
MAD_{anc}	≤6.0°	≤15.0°	≤15.0°	≤15.0°	≤7.0°	
MAD_{free}						≤5.0°
α	≤15.0°	≤15.0°	≤15.0°		≤10.0°	
n_{pTRM}				≥3		
DRAT			≤10.0	≤10.0	≤12.5	
CDRAT				≤11.0		
δCK	≤7	≤9				
δpal	≤10	≤18				
SCAT						TRUE
FRAC						≥0.78
Gap_{max}						≤0.6
DANG						≤10.0°
|k|						≤0.164
k'	<0.35	<0.35	<0.35	<0.35	<0.35	<0.35

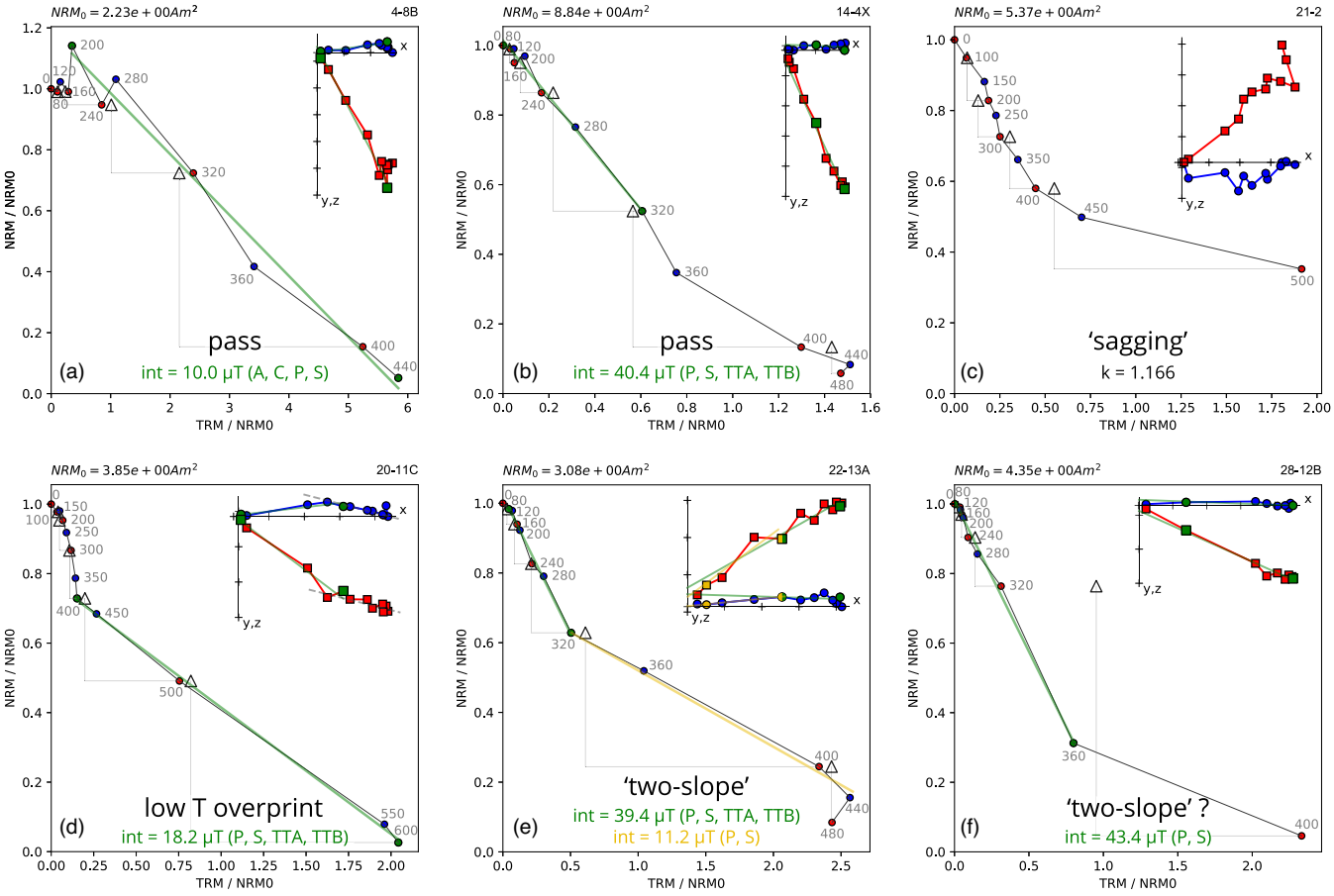

Figure 5. IZZI Thellier results. The IZZI-Thellier results were interpreted using the auto interpreter function of ThellierGUI (Shaar & Tauxe 2013). Many interpretations passed more than one set of selection criteria (e.g. 5A, B, D). C = CROMWELL15, P = PICRIT03 modified, S = SELCRIT02 modified, TTA = ThellierTool A modified, TTB = ThellierTool B modified, A = CLASS A; see also Table 2. 'Sagging' was not uncommon in the IZZI-Thellier results (5C), leading to no interpretations for such a sample. Two-slope behaviour also occurred regularly. When this two-slope behaviour is the result of a low-temperature overprint (5D) the high-temperature part yielded results that pass (one of the sets of) selection criteria; sometimes both slopes produced satisfying results (5E); and when alteration checks fail for the high-temperature segment and the low temperature segment is not overprinted, this low temperature segment may yield successful interpretations (5F).

Downloaded from https://academic.oup.com/gji/article-abstract/215/3/1701/5090145 by Universiteitsbibliotheek Utrecht user on 12 February 2019

Table 3. Palaeointensity data. For each site [with its stratigraphic group (Strat. Gr., U: upper, M: middle, L: lower), and Common True Mean Direction group (CTMD Gr.)], the results of the pseudo-Thellier, multispecimen (MSP), and IZZI-Thellier experiments are provided. For pseudo-Thellier the mean palaeointensity (PI), the associated standard deviation (σ), a measure for scatter in the data (σ/PI), and the number of successful (n) and measured (N) samples are given. Results that arise from <3 samples or are scattered (σ/PI >20 per cent) are not considered reliable and are marked with ∗. For the MSP results the successful protocol [DB or DSC (c for corrected, see main text)], set temperature (T), palaeointensity (PI), with its bootstrapped confidence interval (conf. int.), and number of accepted (n) and measured (N) samples are provided. The IZZI-Thellier results are characterized by the mean palaeointensity (PI), the selection criteria that at least one of the interpretations for a site passes (Sel. crit.: A: class A, P: PICRIT03, S: SELKIN2, TTA, TTB, C: CROMWELL15), the associated standard deviation (σ), a measure for scatter in the data (σ/PI), and the number of interpretations that pass a set of selection criteria (i), with the number of successful (n) and measured (N) samples. Site means that are the result of <3 samples or are scattered (σ/PI >20 per cent) are not considered reliable and are marked with ∗. For the CTMD groups the averages per palaeointensity method are calculated similarly to the averages per site, that is all interpretations that pass from sites within the CTMD group are averaged and their associated standard deviations are calculated.

			Pseudo-Thellier				MSP					IZZI-Thellier				
Site	Strat. Gr.	CTMD Gr.	PI	σ	σ/PI	n (N)	Protocol	T (° C)	PI	Conf. int.	n (N)	PI	Sel. crit.	σ	σ/PI	i/n (N)
EH1	U	1	21.3	0.4	1.9%	5 (5)						*8.6∗*	*A, P, S, TTA, TTB*	*0.2*	*2.2%*	*10/1 (8)*
EH2	U	1	*19.7∗*	–	–	*1 (5)*										
EH3	U	1	22.6	0.5	2.2%	5 (5)						8.3	A, P, S, TTA, TTB	1.3	16.0%	130/6 (10)
EH4	U	1	21.7	0.3	1.4%	4 (5)						8.5	A, P, S, C	1.4	16.8%	145/7 (9)
CTMD1		1	22.1	1.0	4.5%	15 (20)						8.4	A, P, S, TTA, TTB, C	1.4	16.2%	285/14 (27)
EH7	M						DBc	240	28.9	26.1–31.6	6 (10)	*35.8∗*	*P, S, TTA, TTB*	*2.9*	*8.2%*	*10/2 (7)*
EH8I	M		23.4	0.7	3.0%	5 (5)										
EH11	M		38.7	3.5	9.0%	4 (5)						9.6∗	S	–	–	1/1 (10)
EH14			32.6	1.9	5.8%	4 (5)	DSCc	280	23.9	19.1–25.7	6 (9)	40.8	A, P, S, TTA, TTB	5.8	14.2%	77/5 (9)
EH16	L		29.0	2.2	7.6%	5 (5)	DB	220	28.2	26.3–30.0	10 (10)					
EH17	L		27.7	0.3	1.1%	5 (5)	DB	240	32.5	30.9–34.8	7 (10)	*21.1∗*	*A, P, S, TTA, TTB*	*13.1*	*61.2%*	*447/4 (9)*
EH18	L	2	*32.0∗*	*0.2*	*0.6%*	*2 (5)*	DB	240	28.2	25.1–31.3	7 (10)	33.8	A, P, S, TTA, TTB	3.3	9.9%	92/3 (5)
EH19	L	2	32.5	1.7	5.2%	3 (4)						29.4	A, P, S, TTA, TTB	1.3	4.5%	144/4 (9)
EH20	L	2	*30.5∗*	*0.3*	*1.0%*	*2 (5)*						*20.5∗*	*A, P, S, TTA, TTB*	*7.2*	*35.0%*	*70/5 (10)*
CTMD2		2	31.8	2.2	6.9%	7 (14)	DB	240	28.2	25.1–31.3	7 (10)	*28.7∗*		*6.3*	*21.8%*	*306/12 (24)*
EH21	L	3	26.9	2.9	10.8%	3 (5)						*22.4∗*	*P, S, TTB*	*9.3*	*41.6%*	*6/2 (8)*
EH22	L	3	29.3	1.6	5.5%	5 (5)	DSC	260	23.5	21.0–26.0	7 (10)	*27.0∗*	*A, P, S, TTA, TTB*	*13.3*	*49.2%*	*15/2 (9)*
CTMD3		3	28.4	1.8	6.3%	8 (10)	DSC	260	23.5	21.0–26.0	9 (10)	*25.7∗*		*12.2*	*47.7%*	*21/4 (17)*
EH23	L		22.5	1.1	4.9%	5 (5)						*15.5∗*	*P, S, TTB*	*7.5*	*48.6%*	*34/6 (8)*
EH25	L		48.7	0.5	1.0%	5 (5)	DSC	200	18.1	2.4–24.0	8 (10)	61.7	A, P, S, TTA, TTB	11.5	18.6%	148/4 (5)
EH26	L	4					DSCc	200	20.5	16.3–26.3	8 (10)	*25.4∗*	*P, S, TTB*	*2.1*	*8.4%*	*4/2 (6)*
EH27	L	4	32.9	3.0	9.1%	4 (5)						19.2	A, P, S	3.0	15.6%	21/3 (10)
CTMD4		4	32.9	3.0	9.1%	4 (10)	DSCc	200	20.5	16.3–26.3	8 (10)	20.2	A, P, S, TTB	3.7	18.2%	25/5 (16)
EH28	L		35.4	1.7	4.8%	5 (5)	DB	220	28.7	23.7–32.2	9 (10)	*50.8∗*	*P, S*	*10.6*	*20.8%*	*16/2 (10)*
EH29	L											*21.0∗*	*P, S, TTB*	*13.0*	*61.9%*	*17/5 (8)*

Downloaded from https://academic.oup.com/gji/article-abstract/215/3/1701/5090145 by Universiteitsbibliotheek Utrecht user on 12 February 2019

MSP-DSC theory dictates that the line-fit that determines the horizontal axis' cut-off and thereby the palaeointensity, must cross the vertical axis at −1 (Fabian & Leonhardt 2010). A positive ARM test in combination with an MSP-DSC line-fit that has an associated $|\varepsilon_{alt}| > 3.0$ and/or does not cross the vertical axis at −1 within its bootstrap error may be indicative for such progressive alteration. In this particular case we prefer the MSP-DB result since only one heating step is necessary for that protocol, on the notion that this result may very well be slightly too high because of the lack of a domain state correction. The MSP experiment was only carried out for sites that passed the ARM test. The ARM test data were analysed using a custom-made VBA macro. All multispecimen data were analysed using MSP-Tool for Excel 2010, this macro can correct for small alignment errors of the samples' NRM to the applied field in the furnace (Monster *et al.* 2015b).

Fifteen sites were subjected to the ARM test at temperatures ranging from 180 to 350 °C tailored to the alteration temperature of the respective flows (Supplementary Material C). Of these, five passed the test at the first attempted temperature. An additional five sites passed the test at a second, lower temperature. For nine out of these 10 sites, a meaningful MSP palaeointensity could be determined (Fig. 6, Table 3, Supplementary Material D). All accepted MSP palaeointensities are between 18.1 and 32.5 μT. As expected the DSC corrected palaeointensities are lower than those from the DB protocol; downward corrections are between 1.3 and 6.5 μT.

4.3 Pseudo-Thellier method

In the calibrated pseudo-Thellier method (de Groot *et al.* 2013, 2015, 2016; Paterson *et al.* 2016), specimens are demagnetized using alternating fields of increasing strength instead of by heating them to progressively higher temperatures like in the classic Thellier–Thellier style methods. Chemical alteration due to heating is therefore avoided. The first step was AF demagnetization of the samples (Section 3.1). Secondly, the samples were subjected to an ARM acquisition using the same AF steps with a bias field of 40 μT. Finally, the ARM was demagnetized, again at the same field levels. This ARM demagnetization functions as a reliability check: if the ARM is carried by the same grains as the NRM, a plot of the ARM demagnetization against the NRM demagnetization should show a straight line. To find the sample's relative palaeointensity, the NRM remaining after each field step is plotted against the ARM gained during that same step. This relative intensity can be converted to an absolute palaeointensity using the empirical relation arising from data obtained from naturally imparted TRMs (NRMs in volcanic material) between the slope and the palaeointensity: $B_{abs} = 7.718 \cdot$ pseudo-Thellier slope + 14.600 μT (de Groot *et al.* 2016). This calibration formula is valid for a bias field of 40 μT and for samples that have gained half of their maximum ARM (the $B_{1/2ARM}$ value) between 23 and 63 mT. Data were analysed using a custom-made VBA macro for Microsoft Excel 2010.

The calibrated pseudo-Thellier palaeointensity experiment was the most successful of the three methods: 72 specimens (54 per cent) from 18 different sites passed the $B_{1/2ARM}$ selection criterion and showed straight lines in their pseudo-Arai plots (Fig. 7, Table 2 and Supplementary Material E). The obtained palaeointensities were also generally between ∼20 and ∼35 μT. With 38.7 ± 3.5 μT EH11 was slightly higher while EH25 with 48.7 ± 0.5 μT was distinctly higher. Importantly, with the calibrated pseudo-Thellier method also successful palaeointensity could be retrieved from two of the sites that had been partially remagnetized by lightning (EH8I and EH11; respectively 23.4 ± 0.7 and 38.7 ± 3.5 μT). Their overprints were removed by AF fields of ∼15 and ∼10 mT, respectively; calibrated pseudo-Thellier palaeointensity were obtained using the part of the Arai plots between 20 and 100 mT, and 15 and 100 mT, respectively.

5 ^{40}Ar/^{39}Ar DATING

Samples from seven flows at critical points in the stratigraphy (EH1, EH11, EH14, EH17, EH22, EH28 and EH29) were crushed and sieved followed by standard heavy liquid separation to remove minerals such as plagioclase, amphibole and olivine from the groundmass. The size fraction 400–500 μm was hand-picked under a microscope to obtain pure groundmass samples without visible phenocrysts. To remove intergrowths, all samples were leached using a 3 per cent solution of nitric acid. Approximately 0.5 g of groundmass per site was irradiated in CLICIT facility of the OSU Triga reactor at Oregon State University with fast neutrons for one hour. 20 to 30 grains of Fish Canyon sanidine (FCs) were irradiated together with each groundmass sample as a neutron fluence monitor.

After irradiation, samples of ∼30 grains or ∼150 mg were loaded in either 21 or 5 hole Cu trays, respectively and pre-baked for at least 24 hr at 150 °C. Next, samples were placed in an in-house built extraction line and baked for at least 24 hr at 120 °C. The extraction line is equipped with NP10, ST172 and N10 getters, as well as a Ti sponge (used both at room temperature and 500 °C) and a Lauda cold trap set to −60 °C. The gas was gettered for 6 min before being let into the mass spectrometer. Samples were analysed in multicollector mode on a ThermoFisher Helix MC multicollector mass spectrometer at VU University Amsterdam (the Netherlands). ^{40}Ar was measured on the H2 Faraday cup with a 10^{13} Ω amplifier, while ^{39}Ar, ^{38}Ar, ^{37}Ar and ^{36}Ar were measured on respectively the H1, AX, L1 and L2 Compact Discrete Dynode multipliers (CDD). The five detectors were intercalibrated by measuring CO_2 present in the mass spectrometer in dynamic mode. Data were analysed using ArArCALC (Koppers 2002) and custom-made VBA macros to convert Qtegra data to the ArArCALC input format and to calculate and apply the intercalibration correction. Ages were calculated using an age of 28.201 ± 0.046 Ma for Fish Canyon sanidine (Kuiper *et al.* 2008) and Min *et al.* (2000)'s values of the decay constants.

Although optical microscopy did not reveal any minerals that might hamper obtaining a reliable age except for small amounts of volcanic glass, none of the seven sites produced an acceptable plateau or isochron age. Age spectra and isochron plots for EH1, EH11 and EH14 are shown in Fig. 8. Surprisingly, while the age spectra of Samples EH1 and EH11 do not not pass generally accepted criteria for reliability, the obtained 'ages' are broadly in line with what we would expect based on stratigraphic correlation with Széréméta *et al.* (1999)'s section. EH14, on the other hand, is older than would be expected. EH17, EH22, EH28 and EH29 produced even worse age plateaus; isochron spectra are shown in Supplementary Material F.

Part of the lack of reliable age spectra can be attributed to severe peak suppression during the analyses (examples in Supplementary Material F). This implies that we were not able to sufficiently remove contaminants such as water, hydrogen, nitrogen, carbon dioxide and/or hydrocarbons (particularly methane) during the cleaning (gettering) process, leading to unreliable estimates of the amounts of argon in the samples. Adding another getter, heating the Ti sponge to 500 °C and using a Lauda cold trap set to −60 °C improved our measurements somewhat, but unfortunately did not sufficiently reduce the observed peak suppression.

Downloaded from https://academic.oup.com/gji/article-abstract/215/3/1701/5090145 by Universiteitsbibliotheek Utrecht user on 12 February 2019

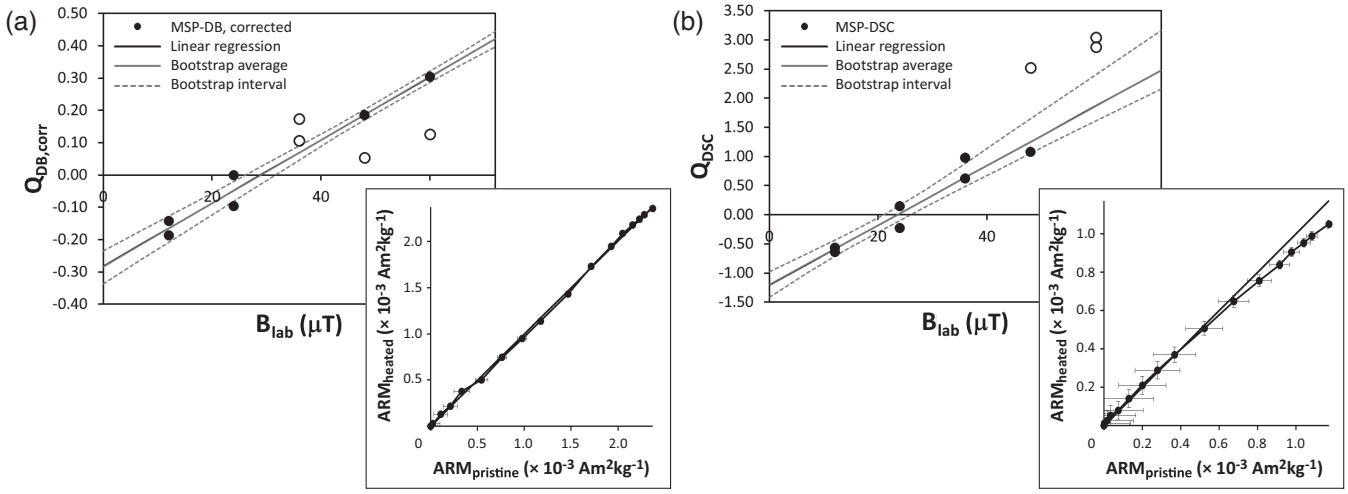

Figure 6. Typical multispecimen (MSP) results. The corrected DB protocol is successful for flow EH7 (a); the DSC protocol yield the best interpretation for site EH22 (b). Both the MSP result (top-left) and the ARM-test (lower-right; de Groot *et al.* 2012) are provided. Both ARM-tests are technically successful since the data plots on the diagonal indicating no change in ARM acquisition behaviour after heating. The *x*-axes intersections of the bootstrapped line fit in the MSP-plots yield the palaeointensity, here 28.9 and 23.5 μT, respectively. Open dots are data points rejected by the bootstrap approach (Monster *et al.* 2015b).

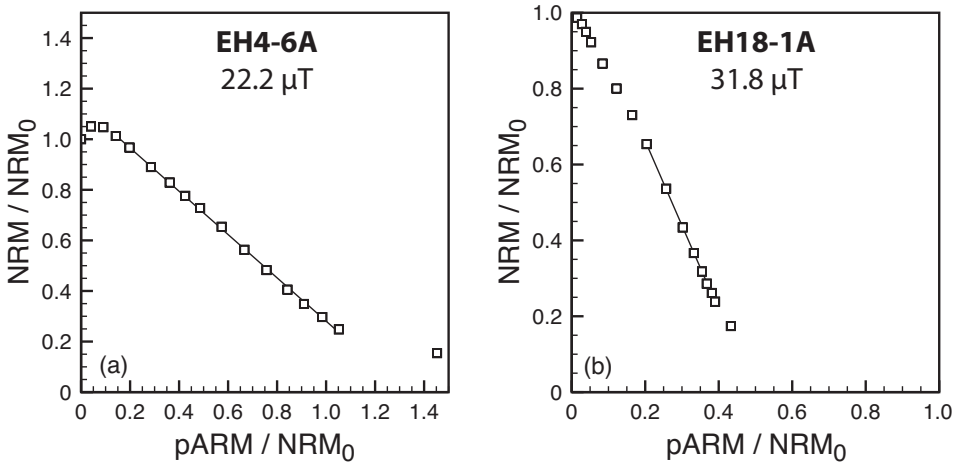

Figure 7. Calibrated pseudo-Thellier results. The pseudo-Thellier slopes are generally very linear, as illustrated by the results of samples EH4-6A (a), and EH18-1A (b). Minor non-linear behaviour is visible for the lower alternating field levels (top left points) and the highest alternating field levels (bottom right points). The most linear segment is interpreted.

6 DISCUSSION

6.1 Quality of the $^{40}Ar/^{39}Ar$ ages

As described in the previous section, contaminants in the sample resulted in peak suppression and thus caused all $^{40}Ar/^{39}Ar$ experiments essentially to fail. Note that some of the older published K–Ar ages (Abdelmonem *et al.* 1972; Fuster 1993) were also argued to be inconsistent by Gillou *et al.* (1996). To identify the source of the contaminants seriously interfering with our dating effort, we heated and gettered sample material using our standard procedures, followed by a peak scan over 0–50 amu (atomic mass units). All samples appeared to contain large amounts of methane (Fig. S1), more than 30 times the amount of ^{40}Ar. The gettering capacity of our system, however, cannot be improved straightforwardly.

The possibility of methane introduction during mineral separation or irradiation procedures can be excluded, since samples from a different volcanic edifice (Terceira, the Azores) that were separated and irradiated in the same batch did not show this behaviour. One would expect possible contaminants introduced during the mineral separation process to be relatively easily removed during prebaking. In addition, samples from the El Golfo sequence on El Hierro studied by Longpré *et al.* (2011) who dated the El Golfo debris avalanche, were also dated in the same VU laboratory on a different extraction line and mass spectrometer, but with a similar gas clean-up and gettering approach. Therefore, the high methane contents have a natural origin related to magmatic processes or to release from the sediment package between the El Hierro edifice and the ocean crust.

Before the actual construction of El Hierro starting at ∼2 Ma an approximately 1-km-thick layer of sediments was deposited on Jurassic-aged ocean crust (e.g. Carracedo & Troll 2016). Note that the ocean between Fuerteventura and Lanzarote and continental Africa where up to 10 km of sediment has accumulated is a prospection target for hydrocarbon exploitation. Eruptive activity could have entrained methane released from the organic matter in

Downloaded from https://academic.oup.com/gji/article-abstract/215/3/1701/5090145 by Universiteitsbibliotheek Utrecht user on 12 February 2019

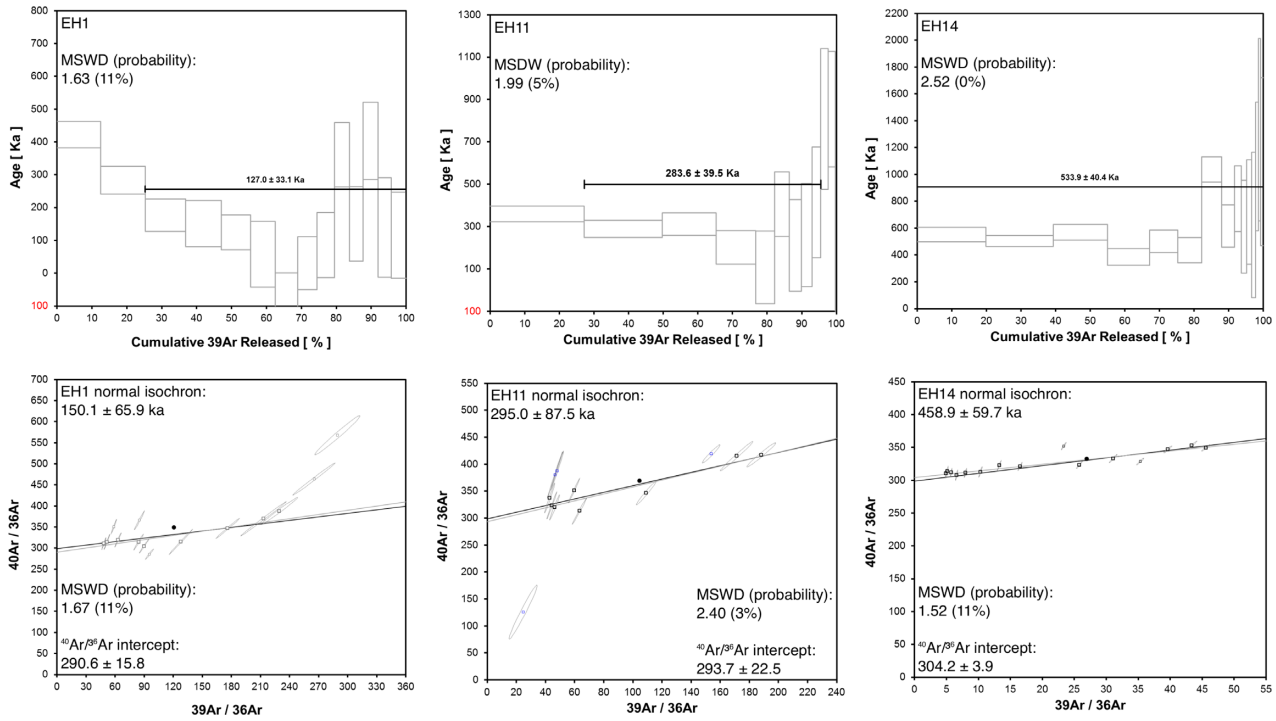

Figure 8. $^{40}Ar/^{39}Ar$ data. Age plateau (top row) and normal isochron (bottom row) for EH1, EH11 and EH14. Plots for the other four sites are provided in Supplementary material F. Uncertainties are given as 2σ. The dashed lines in the plateau plots indicate which steps were used for the age calculation. In the isochron plots, data points corresponding to steps that were used in the plateau are shown in black, whereas discarded data points are shown as smaller grey squares.

the sediments. Abiogenic methane can also form during the serpentinization of ultramafic rocks and subsequently be entrained in the rising magma. Horita & Berndt (1999) conducted experiments under conditions similar to those commonly encountered during serpentinization. It appeared that abiogenic methane forms rapidly under reducing conditions in the presence of even small amounts of Ni-Fe contained in olivine solid solution. Horita & Berndt (1999) therefore suggest that abiogenic methane may be more widespread than commonly thought.

Hernández *et al.* (1998) investigated diffuse emission of CH_4, CO_2 and ^3He in the summit crater of Mt Teide on Tenerife. Their flux measurements indicated a total output of 1.6 tonnes of methane per day. The origin of this methane is uncertain, although low $\delta^{13}C$ values suggest a biogenic contribution (Hernández *et al.* 1998). Experimental results of Horita & Berndt (1999), however, indicate that it is difficult to distinguish between abiogenic and biogenic methane based on isotopic composition. Next to Mt Teide, methane argued to be of abiogenic origin or a mixed biogenic-abiogenic origin has been reported at various locations, such as Precambrian Shield rocks in Canada and South Africa (Sherwood Lollar *et al.* 2006) and serpentinized ultramafic rocks in Turkey (Hosgormez *et al.* 2008) and the Philippines (Abrajano *et al.* 1988).

The methane we observe may thus well be of natural origin. If that is the case, we would expect other K/Ar and $^{40}Ar/^{39}Ar$ studies to have faced similar problems. However, Abdel-Monem *et al.* (1971, 1972), Guillou *et al.* (1996), Széréméta *et al.* (1999) and Longpré *et al.* (2011) do not report peak suppression and/or methane contamination. Furthermore, Guillou *et al.* (1996) and Széréméta *et al.* (1999)'s K/Ar dates are all in stratigraphic order, adding to the reliability of their results. Guillou *et al.* (1996) do state that ages published before 1996 by Abdel-Monem *et al.* (1971, 1972) and Fúster *et al.* (1993) are notably inconsistent, but we do not have sufficient information to link these inconsistencies to methane contaminations. The origin of the methane observed in our samples therefore remains unclear at present. The Camino de Jinama section is closer to the then active volcanic vent than the Camino de la Teña section, so it may have been more prone to methane contamination.

6.2 Age model of the Camino de la Jimana section

Due to the unreliable $^{40}Ar/^{39}Ar$ dating results, we had to rely on stratigraphic correlation using Google Earth (Supplementary material G) and palaeomagnetic correlation with Széréméta *et al.* (1999)'s section. Because of the extensive vegetation cover of rather large parts in the Camino de Jimana section, it was difficult to follow individual flows from one section to the other. Furthermore, the number of big palaeosol levels in the two sections is not equal, complicating correlation attempts.

Comparing the stratigraphic locations of our sites to those of Széréméta *et al.* (1999), it would seem that our Upper Group (EH1 to EH4) and EH6 are most likely part of the Rift Volcanism phase (sites S23-24, S46-65 (S65 is their topmost flow, dated at 134 ± 4 ka) and S1 (lowermost flow, dated at 158 ± 4 ka) of Széréméta *et al.* (1999); we label their flows with 'S' followed by a flow number). The age of EH1 through EH6 would thus be between 134 ± 4 and 158 ± 4 ka. The provisional EH1 age determined in this study, albeit of dubious quality (Fig. 8), supports this correlation. The palaeosol below EH6 may be equivalent to the topmost 'red layer' (naming from the Széréméta *et al.* study) between their S1 and S25 flows, with S25 representing the uppermost flow of the El Golfo phase. Rift volcanism flows in the Camino de la Peña section outnumber those in the Camino de la Jimana section likely because of the wider

Downloaded from https://academic.oup.com/gji/article-abstract/215/3/1701/5090145 by Universiteitsbibliotheek Utrecht user on 12 February 2019

distribution of vents in the Rift Volcanism phase than in the El Golfo phase (Carracedo *et al.* 2001), leading to more local variation.

The tephra deposits between flows EH6 and EH7 could be equivalent to those between S3 and S4. Flow EH7 at the top of our Middle Group (elevation ~950 m) can be traced with some degree of certainty to flow S13 at a height of ~425 m. They appear to share a common true mean direction (CTMD), implying that these may indeed have been erupted around the same time. Our Middle Group could then be placed between 261 ± 6 and 275 ± 6 ka (Széréméta *et al.* 1999). The provisional age obtained for EH11 (284 ± 39 ka, Fig. 8) is in line with this. The thick palaeosol between EH15 and the Lower Group unfortunately cannot be found in Széréméta *et al.* (1999)'s section. Based on stratigraphic correlation, however, it seems likely that the lowest part of our section is more or less equivalent to the lowest part of Széréméta *et al.* (1999)'s section and therefore is not older than ~450 ka.

6.3 Palaeomagnetic secular variation

Declination, inclination and palaeointensity are plotted in stratigraphic order in Fig. 10. Sites with a CTMD are encircled and sites with $k < 50$ have an open symbol. The UG sites (Rift volcanism) represent a spot reading of the field since EH1-4 share a CMTD. EH6 is less reliable ($k < 50$). Therefore we consider further only MG and LG samples. Like Széréméta *et al.* (1999) we observed predominantly easterly directions (Fig. 9, top): 13.7° averaged over all MG and LG samples, compared to 14.2° for Széréméta *et al.* (1999)'s El Golfo sequence. Other PSV data for El Hierro are rather scattered. Watkins (1973) reports average D of 8.5° and I of 47.1° for a set of 35 flows (87 specimens) broadly allocated with a Pleistocene age mainly from the Rift and El Golfo volcanic sequences gauging from their location map. PSV data for La Palma are reported to be conform a geocentric axial dipole field (Tauxe *et al.* 2000). Also the old data set of Watkins (1973) consisting of 21 flows [107 specimens; average (D, I) of 359.5° and 37.6°] supports this inference.

Can the easterly deviation observed for El Hierro be explained by a vertical axis rotation, as suggested by Széréméta *et al.* (1999)? Geologically, a rotation of 15° in less than 450 kyr seems unlikely, as other Canary Islands are not rotated and El Hierro is not located near a strike-slip fault which could have accommodated a local rotation. Other tectonic disturbances, such as the El Golfo flank collapse or the San Andres fault system on the east coast of the island are interpreted to be related to a possibly incipient flank collapse (see e.g. Day *et al.* 1999) and should also be considered. An elusive aspect is that major normal faults which would be related to the El Golfo collapse(s) are not indicated on the geological map of El Hierro. To stay on the safe side, Tauxe *et al.* (2000) did not include data from El Hierro in their database for time-averaged field modelling because of potential tectonic disturbance; they considered especially the El Golfo section suspect.

We should also consider the possibility that the number of sampled flow units undersamples the true palaeosecular variation. Therefore, we applied the A95 test (Deenen *et al.* 2011) to our combined MG and LG (minus site 8I), and the El Golfo data set of Széréméta *et al.* (1999), which are roughly equivalent in age. This test provides an N-dependent A95 envelope (bounded by lower limit $A95_{min} = 12{*}N^{-0.40}$ and upper limit $A95_{max} = 82{*}N^{-0.63}$) that can be used to determine whether a data set has sufficiently sampled palaeosecular variation and therefore represents geomagnetic field behaviour. Here, the aspect that some consecutive flows share a CMTD warrants attention. In essence there are two options: (1)

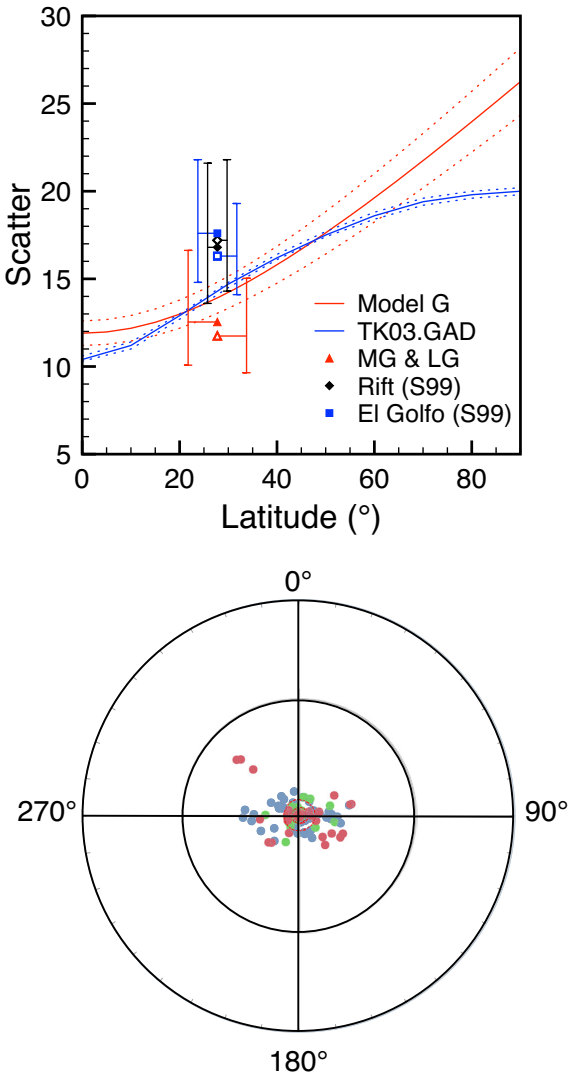

Figure 9. Palaeosecular variation analyses. Top panel: the observed scatter in our combined Middle and Lower Group (red triangles) and Széréméta *et al.* (1999)'s Rift (black diamonds) and El Golfo (blue squares) sections compared to the expected scatter from Model G (McFadden *et al.* 1988) and TK03.GAD (Tauxe & Kent 2004) (A). The observed scatter is generally (just) within error of the expected scatter. The open symbols represent the unfiltered data (all units are counted as individual entries), the solid symbols are the filtered data (units with a CMTD count as a single entry). Bottom panel: the VGP distribution of the unfiltered data of Széréméta *et al.* (1999)'s Rift (in blue) and El Golfo (in red) sections, and our combined Middle and Lower Group (in green). All three data sets show an apparent east–west elongation; the filtered data shows the same trend (not shown).

these flows have been emplaced shortly after each other, that is in ensemble they represent a spot reading of the geomagnetic field or (2) the PSV was indeed low for a given amount of time during which the flows were emplaced. To test between these options Love (1998) suggested that palaeointensity may be used: in absence of directional field variability, the palaeointensity may show substantial variation as indicated by historical field observations. EH1-4, EH18-20, EH21-22 and EH26-27 share CMTDs (Fig. 9) defined as directional averages of consecutive flows being statistically indistinguishable ('A' in the nomenclature of McFadden & McElhinny 1990). CMTD testing was carried out with the Palaeomagnetism.org package (Koymans *et al.* 2016). The CMTD itself is the Fisherian

Downloaded from https://academic.oup.com/gji/article-abstract/215/3/1701/5090145 by Universiteitsbibliotheek Utrecht user on 12 February 2019

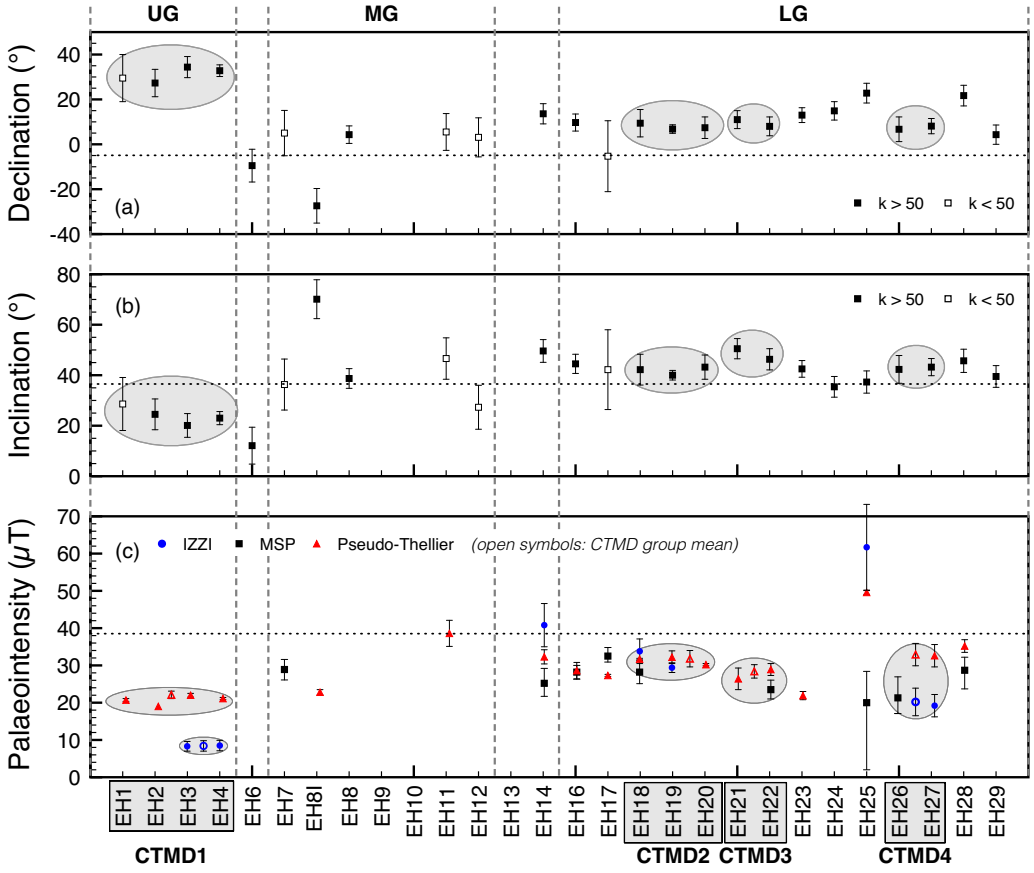

Figure 10. Full-vector geomagnetic information for the Camino de Jinama section. The declination (a), inclination (b) and intensity (c) of the palaeofield are given as a function of site number. The four groups with a Common True Mean Direction (CTMD) are encircled in grey; the palaeointensity results are averaged per method for these CTMD groups (open symbols) and provided in addition to the palaeointensity results per site. The upper (UG), Middle (MG) and Lower Group (LG) are indicated by vertical grey dashed lines. The horizontal dashed lines are the present-day field values (dd. 2015). Error bars refer to standard deviations.

mean of the flows involved. Flows with a CTMD appear to show a similar palaeointensity (Fig. 9), certainly when considering individual palaeointensity protocols. EH18-20 and EH21-22 also show a reasonable between-method coherence; EH1-4 yield remarkably low IZZI Thellier values while EH26-27 show overlapping IZZI and MSP values with notably higher pseudoThellier values. This would plead for those flows being spot readings of the field. For the sake of completeness we show both unfiltered data (all units are counted as individual entries; Fig. 9 open symbols) and filtered data (units with a CMTD count as single entries; Fig. 9 solid symbols).

As explained earlier on the Deenen *et al.* (2011) test calculates the average VGP with scatter envelope for a sample collection. That envelope should be within the sample-number-dependent VGP scatter envelope bounded by $A95_{max}$ and $A95_{min}$. Using the filtered data ($N = 15$), our combined Middle and Lower Group does not pass the Deenen *et al.* (2011) test: the calculated VGP scatter A95 = 3.7° while $A95_{min} = 4.1°$ and $A95_{max} = 14.9°$ (for the unfiltered data ($N = 19$): A95 = 3.0° while $A95_{min} = 3.7°$ and $A95_{max} = 12.8°$). This implies that the determined PSV scatter is lower than that the PSV scatter envelope calculated from the TK03.GAD field model (Tauxe & Kent 2004). Our directional data set thus undersamples true palaeosecular variation as it shows insufficient scatter. Széréméta *et al.* (1999)'s filtered data of the El Golfo section ($N = 28$) barely pass the A95 test (Deenen *et al.* 2011): A95 = 3.3° while $A95_{min} = 3.2°$ and $A95_{max} = 10.0°$ (unfiltered data ($N = 46$): A95 = 2.7°; $A95_{min} = 2.6°$ and $A95_{max} = 7.4°$). Széréméta *et al.* (1999)'s filtered Rift sequence ($N = 17$) shows more scatter: A95 = 6.0° whereas $A95_{min} = 3.9°$ and A95max = 13.8° [unfiltered data ($N = 23$): A95 = 5.9°; $A95_{min} = 3.4°$ and $A95_{max} = 11.4°$]. We also calculated the VGP scatter following McElhinny & McFadden (1997; upper and lower confidence limits from Cox 1970) for our combined Middle and Lower Groups, and Széréméta *et al.* (1999)'s Rift and El Golfo sequences. As is shown in Fig. 9 (top), these values are all within error of the expected scatter from TK03.GAD (Tauxe & Kent 2004) and Model G (McFadden *et al.* 1988; values of a and b from McElhinny & McFadden 1997).

From these latter tests, it would seem that our section and those of Széréméta *et al.* (1999) do properly sample palaeosecular variation. Both tests yield a conflicting outcome, with the A95 failing (merged MG and LG) or barely passing (El Golfo data from Széréméta *et al.* 1999). However, when looking at the VGP distributions of the three sections in Fig. 10 (bottom), the distributions seem elongated (keep in mind that a VGP distribution should be Fisherian in absence of disturbances while direction distributions are always elongated). To illustrate the extent of this VGP elongation, we applied the E/I test for inclination shallowing (Tauxe & Kent 2004; calculations performed in Palaeomagnetism.org; Koymans *et al.* 2016). If these were sedimentary data, the inclination of Széréméta *et al.* (1999)'s filtered El Golfo section would be 'unflattened' from ~38° to ~61°. For the Rift section and our combined Middle and Lower Group,

Downloaded from https://academic.oup.com/gji/article-abstract/215/3/1701/5090145 by Universiteitsbibliotheek Utrecht user on 12 February 2019

the differences between measured and 'unflattened' data are much smaller (3.3° and 7.3°, respectively). We are obviously not dealing with sedimentary data, but the observed elongation does suggest that there has indeed been some form of (tectonic) disturbance. The obtained palaeomagnetic directions should therefore be regarded with caution, and we refrain from making firm inferences about possible vertical axis rotation.

6.4 Palaeointensities: reliability and consistency

An IZZI Thellier flow average could be obtained for 7 out of 28 sites (25 per cent success rate). Ten out of 15 sites showed a positive ARM test; 9 yielded an MSP palaeointensity. Calibrated pseudo-Thellier estimates could be obtained from 18 different flows. The three different palaeointensity methods appear to be broadly supportive of each other (Fig. 10 lowermost panel) given the tedious rock magnetic behaviour during some of the palaeointensity experiments. For site EH16 MSP and calibrated pseudo-Thellier appear to be indistinguishable. EH14 and EH28 have nearly overlapping confidence intervals. EH25 is less successful in this matter. It should be realized that both IZZI-Thellier and MSP come with a large uncertainty envelope for that site. Given its reasonably high calibrated pseudo-Thellier intensity, it seems likely that the field was indeed relatively strong at that moment in time. Sites with only one successful palaeointensity approach yield palaeointensities in line with the others. We now discuss the sites that share a CTMD: EH1-4, EH18-20, EH21-22 and EH26-27. 'Within-method' they all appear to be consistent, strongly suggesting that they represent spot readings of the field. EH18-20 (all three methods), EH21-22 (MSP and calibrated pseudo-Thellier), and EH26-27 (IZZI-Thellier and MSP; calibrated pseudo-Thellier is markedly higher) are also reasonably consistent with overlapping uncertainty envelopes. EH1-4 does not show consistency between the two technically successful approaches: IZZI-Thellier and calibrated pseudo-Thellier markedly differ with the IZZI-Thellier value notably low: just ∼8 μT, while calibrated pseudo-Thellier yields ∼21 μT. This may be due to the current calibration formula used for the pseudo-Thellier results (de Groot *et al.* 2016): this empirical relation does not intersect the origin, hence a pseudo-Thellier slope of 0 results in a palaeointensity of 14.6 μT (see de Groot *et al.* 2016). Palaeointensities of ∼20 μT, however, have been reliably calculated using this calibration formula, but lower palaeointensities cannot be reliably interpreted. The IZZI-Thellier values are therefore probably more reliable for these sites.

A standing question with the multimethods approach is how to come to a single palaeointensity value per cooling unit. If the outcomes of the different methods agree within error, albeit one or two standard deviations, the palaeointensities could be averaged and an associated uncertainty envelope can be calculated. If the palaeointensities produced by a single cooling unit differ, however, it is currently challenging to reject or accept either method over the other, because a theoretical framework on the quality criteria or applicability of the different palaeointensity methods currently lacks. Therefore, averaging palaeointensities that do not agree within error, is dangerous since there is no guarantee that the average is closer to the 'real' palaeointensity than either one of the results of the methods used. We noted earlier (de Groot *et al.* 2016) that the MSP data are often on the lower end of the spectrum, while the IZZI-Thellier data are on the higher end. Here we observe the same trend.

Only the palaeointensity results of sites EH16 and EH18 fully overlap with one standard deviation. Averaging these results yields palaeointensities of 28.6 and 31.0 μT, respectively. Nevertheless, we prefer to report the outcomes of the palaeointensity methods individually, so that when they are used (i.e. as input for a geomagnetic model) they can be accepted, rejected or weighted based on the latest insights.

The obtained palaeointensities range between ∼20 and ∼35 μT is somewhat low compared to the present-day (2015) value of ∼38.5 μT. This is in line with observations from e.g. the East Eifel (Schnepp 1995, 1996; Monster *et al.* 2018) which are broadly coeval. Due to the lack of precise age constraints, it is impossible to compare our data to geomagnetic field models such as PADM2M (Ziegler *et al.* 2011) or palaeointensity stacks such as PISO-1500 (Channell *et al.* 2009) and SINT-800/SINT-2000 (Guyodo & Valet 1999; Valet *et al.* 2005). Converting our range of 20–35 μT to VADMs, however, yields 4.0–7.0 × 10^{22} Am^2, in agreement with the average Brunhes value of 6.2 × 10^{22} Am^2 (Ziegler *et al.* 2011).

7 CONCLUSIONS

Here we presented the first decent full-vector palaeomagnetic record for El Hierro; the palaeointensities were obtained with three independent techniques. For 20 out of 28 sites at least one palaeointensity value could be obtained. When two or more methods were successful for the same site, palaeointensity values appear to have overlapping or nearly overlapping confidence intervals supporting their veracity. Two sites, however, show highly deviating palaeointensity values depending on the technique adopted. These sites we deem not robust. Our palaeointensities are typically between ∼20 and ∼35 μT; when converted to VADMs (4–7 × 10^{22} Am^2), the obtained palaeointensity values are in agreement with average values reported by Ziegler *et al.* (2011) for the Late Quaternary.

The palaeomagnetic declinations obtained for our section are predominantly easterly, deviating by ∼14° from true north, similar to the value obtained by Szériméta *et al.* (1999). The scatter due to palaeosecular variation in our data are within error of the scatter expected from Model G (McFadden *et al.* 1988) and TK03.GAD (Tauxe & Kent 2004) and therefore seems to properly sample palaeosecular variation. Our data, however, do not pass Deenen *et al.* (2011)'s A95 test and Szériméta's data exhibits an elongated VGP distribution. This hints at some undersampling of normal palaeosecular variation, hence the observed easterly deviation in the palaeomagnetic directions may not fully represent the average direction of the Earth's magnetic field. Therefore, we refrain from firm interpretations in the context of a suggested tectonic rotation of the island of El Hierro.

ACKNOWLEDGEMENTS

We thank Manuel Calvo and Elisabeth Schnepp for their thorough and helpful reviews which greatly helped to improve our manuscript. This research was funded by a grant from the Earth and Life Science Division (ALW) of the Netherlands Organization for Scientific Research (NWO). LVdG acknowledges NWO VENI grant 863.15.003. MM would like to thank Daniel Pastor Galán, the Medio Ambiente and Cabildo of El Hierro, and especially Cristina Ferro and Yaneida Quintero González of the Tourist Information Board, for their help in obtaining a permit for sampling.

Downloaded from https://academic.oup.com/gji/article-abstract/215/3/1701/5090145 by Universiteitsbibliotheek Utrecht user on 12 February 2019

REFERENCES

Abdel-Monem, A., Watkins, N.D. & Gast, P.W., 1971. Potassium-argon ages, volcanic stratigraphy, and geomagnetic polarity history of the Canary Islands: Lanzarote, Fuerteventura, Gran Canaria, and La Gomera, *Am. J. Sci.,* **271,** 490–521.

Abdel-Monem, A., Watkins, N.D. & Gast, P.W., 1972. Potassium-argon ages, volcanic stratigraphy, and geomagnetic polarity history of the Canary Islands: Tenerife, La Palma, and El Hierro, *Am. J. Sci.,* **272,** 805–825.

Abrajano, T.A., Sturchio, N.C., Bohlke, J.K. & Lyon, G.L., 1988. Methane-hydrogen gas seeps, Zambales Ophiolite, Philippines: deep or shallow origin? *Chem. Geol.,* **71,** 211–222.

Biggin, A.J., Perrin, M. & Dekkers, M.J., 2007. A reliable absolute palaeointensity determination obtained from a non-ideal recorder, *Earth planet. Sci. Lett.,* **257,** 545–563.

Caccavari, A., Calvo-Rathert, M., Goguitchaichvili, A., Soler, V., He, H. & Vegas, N., 2015. An integrated palaeomagnetic, palaeointensity and $^{40}Ar/^{39}Ar$ investigation on a Miocene polarity transition recorded in a lava sequence in la Gomera, Canary Islands, *Geophys. J. Int.,* **200,** 1297–1316.

Calvo-Rathert, M., Morales-Contreras, J., Carrancho, Á. & Goguitchaichvili, A., 2016. A comparison of Thellier-type and multispecimen paleointensity determinations on Pleistocene and historical lava flows from Lanzarote (Canary Islands, Spain), *Geochem. Geophys. Geosyst.,* **17,** 3638–3654.

Carracedo, J.C., Day, S.J., Guillou, H. & Torrado, F., 1999. Giant Quaternary landslides in the evolution of La Palma and El Hierro, Canary Islands, *J. Volc. Geotherm. Res.,* **94,** 169–190.

Carracedo, J.C., Rodríguez-Badiola, E., Guillou, H., de la Nuez, J. & Pérez Torrado, F.J., 2001. Geology and volcanology of La Palma and El Hierro, Western Canaries, *Estudios Geol.,* **57,** 175–273.

Carracedo, J.C. & Troll, V.R., 2016. *The Geology of the Canary Islands,* xiii + 621 pp. Elsevier.

Carracedo, J.C. *et al.*, 2002. Cenozoic volcanism II: the Canary Islands, in *The Geology of Spain,* pp. 439–472, eds Gibbons, W. & Moreno, T. Geological Society of London.

Channell, J.E.T., Xuan, C. & Hodell, D.A., 2009. Stacking paleointensity and oxygen isotope data for the last 1.5 Myr (PISO-1500), *Earth planet. Sci. Lett.,* **283,** 14–23.

Coe, R.S., 1967. Paleo-intensities of the Earth's magnetic field determined from Tertiary and Quaternary rocks, *J. geophys. Res.,* **72,** 3247–3262.

Cox, A., 1970. Latitude dependence of the angular dispersion of the geomagnetic field, *Geophys. J. R. astr. Soc.,* **20,** 253–269.

Cromwell, G., Tauxe, L., Staudigel, H. & Ron, H., 2015. Paleointensity estimates from historic and modern Hawaiian lava flows using glassy basalt as a primary source material, *Phys. Earth planet. Inter.,* **241,** 44–56.

Day, R., Fuller, M. & Schmidt, V.A., 1977. Hysteresis properties of titanomagnetites—grain-size and compositional dependence, *Phys. Earth planet. Inter.,* **13,** 260–267.

Day, S.J., Heleno da Silva, S.I.N. & Fonseca, J.F.B.D., 1999. A past giant lateral collapse and present-day flank instability of Fogo, Cape Verde Islands, *J. Volc. Geotherm. Res.,* **94,** 191–218.

Deenen, M.H.L., Langereis, C.G., van Hinsbergen, D.J.J. & Biggin, A.J., 2011. Geomagnetic secular variation and the statistics of palaeomagnetic directions, *Geophys. J. Int.,* **186,** 509–520.

de Groot, L.V., Biggin, A.J., Dekkers, M.J., Langereis, C.G. & Herrero-Bervera, E., 2013. Rapid regional perturbations to the recent global geomagnetic decay revealed by a new Hawaiian record, *Nat. Comm.,* **4,** 2727.

de Groot, L.V., Dekkers, M.J. & Mullender, T.A.T., 2012. Exploring the potential of acquisition curves of the anhysteretic remanent magnetization as a tool to detect subtle magnetic alteration induced by heating, *Phys. Earth planet. Inter.,* **194,** 71–84.

de Groot, L.V., Dekkers, M.J., Visscher, M. & ter Maat, G.W., 2014. Magnetic properties and paleointensities as function of depth in a Hawaiian lava flow, *Geochem. Geophys. Geosyst.,* **15,** 1096–1112.

de Groot, L.V., Pimentel, A. & Di Chiara, A., 2016. The multimethod palaeointensity approach applied to volcanics from Terceira: full-vector geomagnetic data for the past 50 kyr, *Geophys. J. Int.,* **206,** 590–604.

de Groot, L.V. *et al.*, 2015. High paleointensities for the Canary Islands constrain the Levant geomagnetic high, *Earth planet. Sci. Lett.,* **419,** 154–167.

Dekkers, M.J. & Böhnel, H.N., 2006. Reliable absolute palaeointensities independent of magnetic domain state, *Earth planet. Sci. Lett.,* **248,** 508–517.

Dunlop, D.J., 2002. Theory and application of the Day plot (Mrs/Ms versus Hcr/Hc) 1. Theoretical curves and tests using titanomagnetite data., *J. Geophys. Res.,* **107,** 2056.

Fabian, K. & Leonhardt, R., 2010. Multiple-specimen absolute paleointensity determination: an optimal protocol including pTRM normalization, domain-state correction, and alteration test, *Earth planet. Sci. Lett.,* **297,** 84–94.

Fullea, J., Camacho, A.G., Negredo, A.M. & Fernández, J., 2015. The Canary Islands hot spot: new insights from 3D coupled geophysical-petrological modelling of the lithosphere and uppermost mantle, *Earth planet. Sci. Lett.,* **409,** 71–88.

Fúster, J.M., Hernán, F., Cendrero, A., Coello, J., Canragrel, J.M., Ancochea, E. & Barrola, E., 1993. Geochronologia de la Isla de El Hierro Islas Canarias, *Bol. R. Soc. Esp. Hist. Nat. Sec. Geol.,* **88,** 85–97.

Gee, M., Watts, A.B., Masson, D.G. & Mitchell, N.C., 2001. Landslides and the evolution of El Hierro in the Canary Islands, *Mar. Geol.,* **177,** 271–293.

Guillou, H., Carracedo, J.C., Torrado, F.P. & Badiola, E.R., 1996. K-Ar ages and magnetic stratigraphy of a hotspot-induced, fast grown oceanic island: El Hierro, Canary Islands, *J. Volc. Geotherm. Res.,* **73,** 141–155.

Guyodo, Y. & Valet, J.-P., 1999. Global changes in intensity of the Earth's magnetic field during the past 800 kyr, *Nature,* **399,** 249–252.

Hernández, P.A., Pérez, N.M., Salazar, J.M., Nakai, S., Notsu, K. & Wakita, H., 1998. Diffuse emission of carbon dioxide, methane, and helium-3 from Teide Volcano, Tenerife, Canary Islands, *Geophys. Res. Lett.,* **25,** 3311–3314.

Hoernle, K., Tilton, G. & Schmincke, H.U., 1991. Sr-Nd-Pb isotopic evolution of Gran Canaria: evidence for shallow enriched mantle beneath the Canary Islands, *Earth planet. Sci. Lett.,* **106,** 44–63.

Holik, J.S., Rabinowitz, P.D. & Austin, J.A., 1991. Effects of Canary hotspot volcanism on structure of oceanic crust off Morocco, *J. geophys. Res.,* **96**(B7), 12 039–012 067.

Horita, J. & Berndt, M.E., 1999. Abiogenic methane formation and isotopic fractionation under hydrothermal conditions, *Science,* **285,** 1055–1057.

Hosgormez, H., Etiope, G. & Yalçin, M.N., 2008. New evidence for a mixed inorganic and organic origin of the Olympic Chimaera fire (Turkey): a large onshore seepage of abiogenic gas, *Geofluids,* **8,** 263–273.

Kissel, C., Guillou, H., Laj, C., Carracedo, J.C., Perez-Torrado, F., Wandres, C., Rodriguez-Gonzalez, A. & Nomade, S., 2014. A combined paleomagnetic/dating investigation of the upper Jaramillo transition from a volcanic section at Tenerife (Canary Islands), Earth Planet, *Sci. Lett.,* **406,** 59–71.

Kissel, C. & Laj, C., 2004. Improvements in procedure and paleointensity selection criteria (PICRIT-03) for Thellier and Thellier determinations: application to Hawaiian basaltic long cores, *Phys. Earth planet. Inter.,* **147,** 155–169.

Kissel, C., Laj, C., Rodriguez-Gonzalez, A., Perez-Torrado, F., Carracedo, J.C. & Wandres, C., 2015. Holocene geomagnetic field intensity variations: contribution from the low latitude Canary Islands site, *Earth planet. Sci. Lett.,* **430,** 178–190.

Knudsen, M.F., Riisager, P., Donadini, F., Snowball, I., Muscheler, R., Korhonen, K. & Pesonen, L.J., 2008. Variations in the geomagnetic dipole moment during the Holocene and the past 50 kyr, *Earth planet. Sci. Lett.,* **272,** 319–329.

Koppers, A.A.P., 2002. ArArCALC—software for $^{40}Ar/^{39}Ar$ age calculations, *Comp. Geosci.,* **28,** 605–619.

Korte, M., Constable, C., Donadini, F. & Holme, R., 2011. Reconstructing the Holocene geomagnetic field, *Earth planet. Sci. Lett.,* **312,** 497–505.

Downloaded from https://academic.oup.com/gji/article-abstract/215/3/1701/5090145 by Universiteitsbibliotheek Utrecht user on 12 February 2019

Korte, M., Donadini, F. & Constable, C.G., 2009. Geomagnetic field for 0–3 ka: 2. A new series of time-varying global models, *Geochem. Geophys. Geosyst.,* **10,** Q06008.

Koymans, M.R., Langereis, C.G., Pastor-Galán, D. & van Hinsbergen, D.J.J., 2016. Paleomagnetism.org: an online multi-platform open source environment for paleomagnetic data analysis, *Comp. Geosci.,* **93,** 127–137.

Kuiper, K.F., Deino, A., Hilgen, F.J., Krijgsman, W., Renne, P.R. & Wijbrans, J.R., 2008. Synchronizing rock clocks of Earth history, *Science,* **320,** 500–504.

Lawrence, K.P., Tauxe, L., Staudigel, H., Constable, C.G., Koppers, A., McIntosh, W. & Johnson, C.L., 2009. Paleomagnetic field properties at high southern latitude, Geochem, *Geophys. Geosyst.,* **10,** Q01005.

Leonhardt, R., Heunemann, C. & Krása, D., 2004. Analyzing absolute paleointensity determinations: acceptance criteria and the software ThellierTool4.0, *Geochem. Geophys. Geosyst.,* **5,** Q12016.

Longpré, M.-A., Chadwick, J.P., Wijbrans, J.R. & Iping, R., 2011. Age of the El Golfo debris avalanche, El Hierro (Canary Islands): new constraints from laser and furnace ^{40}Ar/ ^{39}Ar dating, *J. Volc. Geotherm. Res.,* **203,** 76–80.

Love, J.J., 1998. Paleomagnetic volcanic data and geomagnetic regularity of reversals and excursions, *J. geophys. Res.,* **103,** 12435–12452.

Masson, D.G., 1996. Catastrophic collapse of the volcanic island of Hierro 15 ka ago and the history of landslides in the Canary Islands, *Geology,* **24,** 231–234.

Masson, D.G., Watts, A.B., Gee, M., Urgeles, R., Mitchell, N.C., Le Bas, T.P. & Canals, M., 2002. Slope failures on the flanks of the western Canary Islands, *Earth Sci. Rev.,* **57,** 1–35.

McElhinny, M.W. & McFadden, P.L., 1997. Palaeosecular variation over the past 5 Myr based on a new generalized database, *Geophys. J. Int.,* **131,** 240–252.

McFadden, P.L. & McElhinny, M.W., 1990. Classification of the reversal test in palaeomagnetism, *Geophys. J. Int.,* **103,** 725–729.

McFadden, P.L., Merrill, R.T. & McElhinny, M.W., 1988. Dipole/Quadrupole family modeling of paleosecular variation, *J. geophys. Res.,* **93,** 11583–11588.

Min, K., Mundil, R., Renne, P.R. & Ludwig, K.R., 2000. A test for systematic errors in 40Ar/39Ar geochronology through comparison with U/Pb analysis of a 1.1-Ga rhyolite, *Geochim. cosmochim. Acta.,* **64,** 73–98.

Monster, M.W.L., de Groot, L.V., Biggin, A.J. & Dekkers, M.J., 2015a. The performance of various palaeointensity techniques as a function of rock magnetic behaviour – a case study for La Palma, *Phys. Earth planet. Inter.,* **242,** 36–49.

Monster, M.W.L., de Groot, L.V. & Dekkers, M.J., 2015b. MSP-Tool: a VBA-based software tool for the analysis of multispecimen paleointensity data, *Front. Earth Sci.,* **3,** 86.

Monster, M.W.L., Langemeijer, J., Wiarda, L.R., Dekkers, M.J., Biggin, A.J., Hurst, E.A. & de Groot, L.V., 2018. Full-vector geomagnetic field records from the East Eifel, Germany, *Phys. Earth planet. Inter.,* **274,** 148–157.

Mullender, T.A.T., Frederichs, T., Hilgenfeldt, C., de Groot, L.V., Fabian, K. & Dekkers, M.J., 2016. Automated rock magnetic data acquisition with an in-line horizontal '2G' system, *Geochem. Geophys. Geosyst.,* **17,** 3546–3559.

Paterson, G.A., 2011. A simple test for the presence of multidomain behavior during paleointensity experiments, *J. geophys. Res.,* **116,** B10104.

Paterson, G.A., Heslop, D. & Pan, Y., 2016. The pseudo-Thellier palaeointensity method: new calibration and uncertainty estimates, *Geophys. J. Int.,* **207,** 1596–1608.

Paterson, G.A., Tauxe, L., Biggin, A.J., Shaar, R. & Jonestrask, L.C., 2014. On improving the selection of Thellier-type paleointensity data, *Geochem. Geophys. Geosyst.,* **15,** 1180–1192.

Quidelleur, X., Gillot, P.-Y., Carlut, J. & Courtillot, V., 1999. Link between excursions and paleointensity inferred from abnormal field directions recorded at La Palma around 600 ka, *Earth planet. Sci. Lett.,* **168,** 233–242.

Quidelleur, X. & Valet, J.-P., 1996. Geomagnetic changes across the last reversal recorded in lava flows from La Palma, Canary Islands, *J. geophys. Res.,* **101,** 13755–13773.

Schnepp, E., 1995. Palaeointensity study of Quaternary East Eifel phonolitic rocks (Germany), *Geophys. J. Int.,* **121,** 627–633.

Schnepp, E., 1996. Geomagnetic paleointensities derived from volcanic rocks of the Quaternary East Eifel volcanic field, Germany, *Phys. Earth planet. Inter.,* **94,** 23–41.

Shaar, R. & Tauxe, L., 2013. Thellier GUI: an integrated tool for analyzing paleointensity data from Thellier-type experiments, *Geochem. Geophys. Geosyst.,* **14,** 677–692.

Sherwood Lollar, B., Lacrampe-Couloume, G., Slater, G.F., Ward, J., Moser, D.P., Gihring, T.M., Lin, L.H. & Onstott, T.C., 2006. Unravelling abiogenic and biogenic sources of methane in the Earth's deep subsurface, *Chem. Geol.,* **226,** 328–339.

Singer, B.S., Relle, M.K. & Hoffman, K.A., 2002. Ar/Ar ages from transitionally magnetized lavas on La Palma, Canary Islands, and the geomagnetic instability timescale, *J. geophys. Res.,* **107,** EPM 7–1-EPM 7-20.

Soler, V., Carracedo, J.C. & Heller, F., 1984. Geomagnetic secular variation in historical lavas from the Canary-Islands, *Geophys. J. R. astr. Soc.,* **78,** 313–318.

Széréméta, N., Laj, C., Guillou, H., Kissel, C., Mazaud, A. & Carracedo, J.C., 1999. Geomagnetic paleosecular variation in the Brunhes period, from the island of El Hierro (Canary Islands), *Earth planet. Sci. Lett.,* **165,** 241–253.

Tauxe, L. & Kent, D.V., 2004. A simplified statistical model for the geomagnetic field and the detection of shallow bias in paleomagnetic inclinations: was the ancient magnetic field dipolar? in *Geophysical Monograph Series, Geophysical Monograph Series,* pp. 101–115, American Geophysical Union.

Tauxe, L. & Love, J.J., 2003. Paleointensity in Hawaiian Scientific Drilling Project Hole (HSDP2): results from submarine basaltic glass, *Geochem., Geophys., Geosyst.,* **4,** 8702.

Tauxe, L. & Staudigel, H., 2004. Strength of the geomagnetic field in the Cretaceous Normal Superchron: new data from submarine basaltic glass of the Troodos Ophiolite, *Geochem. Geophys. Geosyst.,* **5,** Q02H06.

Tauxe, L., Staudigel, H. & Wijbrans, J., 2000. Paleomagnetism and ^{40}Ar/^{39}Ar ages from La Palma in the Canary Islands, *Geochem. Geophys. Geosyst.,* **1,** 2000GC000063.

Valet, J., Meynadier, L. & Guyodo, Y., 2005. Geomagnetic dipole strength and reversal rate over the past two million years, *Nature,* **435,** 802–805.

Valet, J.P., Brassart, J., Quidelleur, X., Soler, V., Gillot, P.Y. & Hongre, L., 1999. Paleointensity variations across the last geomagnetic reversal at La Palma, Canary Islands, Spain, *J. geophys. Res.,* **104,** 7577–7598.

van den Bogaard, P., 2013. The origin of the Canary Island Seamount Province—new ages of old seamounts, *Sci. Rep.,* 3, art. number 2107.

Watkins, N.D., 1973. Paleomagnetism of the Canary Islands and Madeira, *Geophys. J. R. astr. Soc.,* **32,** 249–267.

Watkins, N.D. & Haggerty, S.E., 1968. Oxidation and Magnetic Polarity in Single Icelandic Lavas and Dikes, *Geophys. J. Int.,* **15,** 305–315.

Yu, Y.J. & Tauxe, L., 2005. Testing the IZZI protocol of geomagnetic field intensity determination, *Geochem. Geophys. Geosyst.,* **6,** Q05H17.

Ziegler, L.B., Constable, C.G., Johnson, C.L. & Tauxe, L., 2011. PADM2M: a penalized maximum likelihood model of the 0–2 Ma palaeomagnetic axial dipole moment, *Geophys. J. Int.,* **184,** 1069–1089.

Ziegler, L.B., Constable, C.G. & Johnson, C.L. 2008. Testing the robustness and limitations of 0–1 Ma absolute paleointensity data, *Phys. Earth planet. Inter.,* **170,** 34–45.

SUPPORTING INFORMATION

Supplementary data are available at *GJI* online.

Figure A1. Day plot, showing Mrs/Ms plotted against Bcr/Bc. The SD + MD mixing lines (Dunlop 2002) are shown in grey.

Figure F1ab. Four specimens passed the $B_{1/2ARM}$ and linearity criteria. EH1-9B was not taken into account.

Downloaded from https://academic.oup.com/gji/article-abstract/215/3/1701/5090145 by Universiteitsbibliotheek Utrecht user on 12 February 2019

Figure F2ab. Only EH2-4A passed the $B_{1/2ARM}$ criterion.
Figure F3ab. Sample EH3-6A shows an overprint. Otherwise homogeneous data.
Figure F4ab. Specimen EH4-3A fails the B1/2ARM criterion.
Figure F5ab. All specimens fail the B1/2ARM criterion and show non-linear behaviour.
Figure F6ab. All specimens fail the B1/2ARM criterion and show non-linear behaviour.
Figure F7ab. These specimens show a lightning-induced overprint at low AF fields (<20 mT).
Figure F8ab. Except for EH11-11A, all specimens passed the B1/2ARM criterion and show linear behaviour.
Figure F9ab. All specimens fail the B1/2ARM criterion.
Figure F10ab. EH14-11A was not taken into account due to non-linearity.
Figure F11ab. All specimens passed the B1/2ARM and linearity criteria.
Figure F12ab. All specimens passed the B1/2ARM and linearity criteria.
Figure F13ab. Only two specimens passed the B1/2ARM and linearity criteria.
Figure F14ab. Three out of four specimens passed the B1/2ARM and linearity criteria.
Figure F15ab. All specimens passed the B1/2ARM and linearity criteria.
Figure F16ab. Three specimens passed the B1/2ARM and linearity criteria.
Figure F17ab. All specimens passed the B1/2ARM and linearity criteria.
Figure F18ab. All specimens passed the B1/2ARM and linearity criteria. EH23-12A shows an overprint.
Figure F19ab. All specimens failed the B1/2ARM and linearity criteria.
Figure F20ab. All specimens passed the B1/2ARM and linearity criteria.
Figure F21ab. All specimens failed the B1/2ARM criterion.
Figure F22ab. EH27-9A was not taken into account in the average because its B1/2ARM <23.
Figure F23ab. All specimens passed the B1/2ARM and linearity criteria.
Figure F24ab. All specimens failed the B1/2ARM criterion.
Fig. G1 Peak scan from atomic mass 0 to 50 u. The methane signal at c. 16 u is c. 100 times larger than the ^{40}Ar signal. Because of this large amount of methane, the ionization process was often incomplete, leading to peak suppression.
Fig. G2 ^{40}Ar signal as measured on the Helix MC. These results are from the first measurement of these samples. In later measurements, more getters were employed to better filter out contaminants such as methane and thus reduce the amount of peak suppression. **Left:** This heating step of site EH1 shows severe peak suppression. **Right:** In this case (site EH29), a regression can be calculated through the last 9 data points.
Fig. G3 Age plateau, K/Ca plateau, normal isochron and inverse isochron for site EH1, adapted from ArArCALC-generated plots. This site shows no real plateau and rather noisy isochrons. The smaller squares in the isochrons represent the discarded steps.
Fig. G4 Age plateau, K/Ca plateau, normal isochron and inverse isochron for site EH11, adapted from ArArCALC-generated plots. The smaller squares in the isochrons represent the discarded steps.
Fig. G5a Age plateau, K/Ca plateau, normal isochron and inverse isochron for site EH14, adapted from ArArCALC-generated plots. The smaller squares in the isochrons represent the discarded steps.
Fig. G6 Age plateau, K/Ca plateau, normal isochron and inverse isochron for site EH17, adapted from ArArCALC-generated plots. The smaller squares in the isochrons represent the discarded steps.
Fig. G7 Age plateau, K/Ca plateau, normal isochron and inverse isochron for site EH22, adapted from ArArCALC-generated plots. The smaller squares in the isochrons represent the discarded steps.
Fig. G8 Age plateau, K/Ca plateau, normal isochron and inverse isochron for site EH28, adapted from ArArCALC-generated plots. The smaller squares in the isochrons represent the discarded steps.
Fig. G9 Age plateau, K/Ca plateau, normal isochron and inverse isochron for site EH29, adapted from ArArCALC-generated plots. The smaller squares in the isochrons represent the discarded steps.
Figure H1. Stratigraphic correlation between our section along Camino de Jinama (in red) and Széréméta *et al.* (1999)'s section along Camino de la Teña (in yellow). Image created using Google Earth. The 'wobbles' in some of the white lines are due to the software.
Supp_mat_optimized_reduced_R1.pdf
Supp_Table_IZZI.pdf

Please note: Oxford University Press is not responsible for the content or functionality of any supporting materials supplied by the authors. Any queries (other than missing material) should be directed to the corresponding author for the article.

Downloaded from https://academic.oup.com/gji/article-abstract/215/3/1701/5090145 by Universiteitsbibliotheek Utrecht user on 12 February 2019